Simulating Flexible Origami Structures
by Finite Element Method

Y.C.Hu[1,2], Y.X.Zhou[1,3], K.W.Kwok[1], K.Y.Sze[1*]

1 Dept. of Mechanical Engineering, The University of Hong Kong, Pokfulam, Hong Kong, China.

2 Dept. of Mechanics & Aerospace Engineering, Southern University of Science & Technology, Shenzhen, China.

3 Faculty of Science, Harbin Institute of Technology (Shenzhen), Shenzhen, China.

* Corresponding Author, Email: kysze@hku.hk

ABSTRACT

Most origamis are composed of triangular and quadrilateral facets. Since creases are practically straight, facets can be modelled as 3-node triangles (T3) and 4-node quadrilaterals (Q4) with translational nodal dofs only. While bending is not possible in T3, a corotational consideration is employed to quantify the bending deformation in Q4 under large displacement/rotation but small strain/curvature. The pertinent tangential stiffness matrix turns out to be a simple constant matrix. Meanwhile, the fold angle of the crease is computed by the dot product of two vectors connecting the crease and nodes defining the adjacent facets. Derivatives of the fold angle are considerably simplified by invoking the small strain/curvature behaviour of the facet. To manoeuver the origami from its initial to final configuration, rest angles defining the zero energy states of the creases are changed to their target values incrementally. The proposed methods of quantifying the bending deformation in Q4 and the derivative of the fold angle are implemented in a commercial software using two user-defined element subroutines. They together with the built-in 3D membrane elements realize the simulation and analysis of origami in a finite element environment. Furthermore, the element for modelling the crease is equally applicable to modelling spring-loaded hinges.

Keywords: origami; corotational method; finite element; crease; fold angle; elastic hinge.

1. INTRODUCTION

Origami is an art of paper folding that turns flat pieces of paper into 3D structures. Origamis exhibit interesting shape morphing and have inspired numerous applications in engineering such as deployable space solar sails (Miura 1985; Zirbel et al. 2013), novel mechanisms (Zhang and Chen 2018; Nelson et al. 2019), energy-absorbing devices (Ma and You 2013; Lee et al. 2019), meta-materials (Schenk and Guest 2013; Zhai et al. 2018; Pratapa et al. 2019), etc. To date, polyhedral origamis composing of triangular and quadrilateral facets are most widely used in engineering. The deformation of origami involves that of the facet and crease folding. General speaking, the facet undergoes large displacement large rotation but small strain and, if possible, small curvature. To simulate the origami deformation, a classical approach is to adopt the rigid facet assumption in which only crease folding is allowed (Tachi 2009; Wei et al. 2013). The deformed configuration can be obtained efficiently at the expense of setting up geometric constraints which often requires a high level of mathematical skill. Recent emphasis on origami modelling is on deformable facets and elastic creases. The finite element method widely used in the structural analysis has been considered in crushing analysis and the facets can readily be modelled as plate/shell elements (Ma et al. 2018; Song et al. 2012). However, there are a few obstacles for analyzing origamis which can fold and unfold repeatedly using the finite element method.

Firstly, plate/shell elements with rotation dofs are quite often slow in convergence in large rotation analyses, probably because finite rotation is not commutative and special treatment is required to update the rotation (Crisfield 2000). Partly because of this reason and partly because 3D constitutive models can be directly adopted, considerable research effort has gone into solid-shell elements (Park et al. 1995; Kim and Lee 1988; Bischhoff and Ramm 1998; Hauptmann and Schweizerhof 1998; Sze et al. 2002; Sze 2002; Kim et al. 2003, Bischoff et al. 2018; Kulikov and Plotnikova 2008) and other rotation-free elements (Guo et al. 2002; Flores and Oñate 2011; Zhou and Sze 2012) which possess only translational dofs. As an illustration, the popular benchmark problem in which a slit annular plate with inner radius 6 and outer radius 10 (Sze et al. 2004) meshed into 6×30 elements is analyzed by using the four-node shell element models S4 and S4R as well as the 8-node solid-shell element model SC8R of ABAQUS. A line force is applied at the free end of the radial slit while the other end of the slit is fully clamped. Fig. 1 shows the undeformed and the final deformed configurations at the maximum line force at 0.8 unit of force per unit length. The default time increment in ABAQUS is adopted, i.e., the initial, minimum, and largest time increment sizes are 1, 10^{-5}, and 1, respectively. The default automatic time increment option, see the first paragraph in Section 5, is employed. The analyses were conducted in a laptop PC with Intel(R) Core(TM) i9-9880H CPU (8 cores, 2.30 GHz) and 64 GB RAM. The predictions of S4, S4R and SC8R are practically identical. The analysis data are given in Table 1. It can be seen that SC8R consumed far less number of time increments, number of iterations and CPU time than the S4 and S4R shell element models. Another example comparing S4R and SC8R can also be found in Section 5.1.
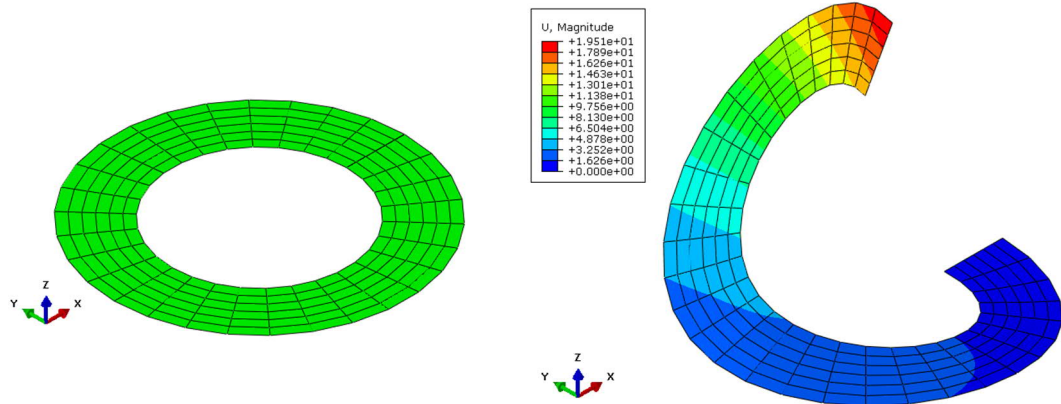
Figure 1 (a) The undeformed and (b) the final deformed mesh of the slit annular plate problem. The thickness, elasticity modulus and Poisson's ratio of the plate are 0.03, 21×10^6 and 0, respectively.

Table 1. Analysis data for different element models in the slit annular plate problem in Figure 1.

	Total no. of time increments	Total no. of iterations	CPU time	The first time increment*	The smallest time increment
S4	58	409	9.9 sec	0.00390625	0.00390625
S4R	64	913	15.0 sec	0.015625	0.000976563
SC8R	27	186	3.6 sec	0.0625	0.0263672

* This is the first time increment using which the convergence can be attained.

Secondly, the elastic hinge needed for modelling the elastic crease is not readily available in most, if not all, commercial finite element programs. Taking ABAQUS as an example, it provides 3 types of spring elements, i.e., SPRING1, SPRING2 and SPRINGA. SPRING1 is a grounded spring defined by only one globally or locally defined dofs. SPRING2 can connect any two globally or locally defined dofs. In principle, an elastic hinge can be realized by coupling two local rotations defined about the hinge using SPRING2. However, ABAQUS requires the local coordinate system used to define the local rotation to be fixed even in large displacement analysis. However, creases in origamis undergoing large displacement and their orientations vary. SPRINGA can adopt the line between two end nodes as the axis which can rotate and translate in large displacement analysis but it can only model extensional/compressive springs.

Thirdly, modelling origami with plate/shell elements with rotational dofs will couple the nodal rotations and the hinge angles. A possible workaround is to define the nodes of adjacent plate/shell elements at the same crease vertex and constrain the equality of the nodal translations. The drawback of this approach can be understood by considering, e.g., a crease vertex shared by 4 facets. While the 3×4 translational dofs can be trimmed down to 3 by constraints, the 3×4 rotational dofs remain active. In the origami simulation methods to be reviewed below, there are only 3 translation dofs per node. The impact of using 15 instead of 3 dofs per crease vertex on the computational efficiency can be considerable.

The bar-hinge approach can be regarded as a simplified finite element method which can consider deformable facets and elastic creases (Schenk and Guest 2011). In the model, the origami is first

3

represented by a network of bar or truss elements along creases with the element nodes at the endpoints of creases only. Without introducing additional nodes, quadrilateral or higher-order polyhedral facets are then divided into triangles by additional bar elements. The membrane deformation, also known as the shearing/stretching deformation and in-plane deformation, is accounted for by the axial deformation of the bar elements. All inter-facet and intra-facet bar elements are also elastic hinges whilst the stiffness of the latter is derived from the bending stiffness of facets, respectively (Schenk and Guest 2011; Filipov et al. 2017; Gillman et al. 2018). The dihedral angle of the crease is an inverse sine or cosine function of the displacements at nodes defining the adjacent facets. Thus, derivatives of the dihedral angle contain the cosine or sine function in the denominator. The 0/0, zero divided by zero, points need to be removed by expressing the derivatives using algebraic terms (Liu and Paulino 2017; Schenk and Guest 2011; Bekker 1996). To avoid the complication, the *arctan2* function, instead of *arccos* or *arcsin* functions, was also suggested for computing the dihedral angle at the expense of using two arguments in the function (Gillman et al. 2018). To trace the large displacement which may involve bistability and bifurcations, advanced solution techniques have also been incorporated into the bar-hinge models. Other features such as material nonlinearity, fold stiffness with penalty near the fully-folded state to avoid penetration can also be noted (Liu and Paulino 2017; Gillman et al. 2018). Recently, the bar-hinge models have been adopted to uncover some unique mechanistic properties of the origami structures (Grey et al. 2019; Liu et al. 2019).

This paper develops a simplified FEM approach in which the origami is modelled by *ad hoc* developed bending and elastic crease elements. Since origamis with pentagonal and higher-order polygonal facets are seldom used in engineering applications, triangular and quadrilateral facets are considered here. Each of these facets would be modelled by 3-node triangle (T3) or 4-node quadrilateral (Q4) with only translational nodal dofs. The membrane deformation in T3 and Q4 can be accounted for by any geometric nonlinear 3D membrane elements of the same nodal configurations. Since creases are practically straight due to the large membrane stiffness of the adjacent non-coplanar facets, bending deformation is not possible in T3 facet whilst there is only one bending deformation mode in the Q4 facet. In this light, a Q4 bending element is developed based on the corotational concept. Under the large-displacement, large-rotation but small strain small curvature assumption, it will be shown that the bending deformation mode can be quantified by the distance between the two straight lines connecting the opposite corners of the quadrilateral. A point of remark is that the two straight lines lie on the flat Q4 facet but would detach from the facet when the facet becomes curved. The salient feature of the elastic energy in the Q4 bending element is that it is quadratic in nodal displacements. Thus, the pertinent tangential stiffness matrix is a constant which does not needs to be updated in the iterative solution process. For the elastic energy in the crease, a 4-node crease element is derived in which the dot product of two vectors connecting the crease and the adjacent nodes are used to determine the fold angle which is the complement of the dihedral angle of the crease. A similar way of computing the dihedral angle can be noted in (Bekker 1996). Here, the large-displacement but small-strain and small-curvature assumption for the facet is invoked to simplify the derivatives of the fold angle with respect to the nodal

displacement. The 4-node crease element is equally applicable to model elastic hinges or, equivalently, hinges loaded with torsional springs. To manoeuver the origami into its deformed configuration, the rest angles which define the zero elastic energy states of the creases are changed to their target values incrementally.

The presented Q4 bending element and the 4-node crease element are implemented in ABAQUS thru two user-defined element subroutines. They together with the nonlinear T3 and Q4 3D membrane elements in ABAQUS realize the origami simulation in a finite element environment. Examples are presented to validate the two developed elements for modelling elastic hinges, origami, and kirigami structures.

2. FACET MODELLING

It will be assumed as in the bar-hinge approach that creases are straight and nodes carrying the dofs in the computation are located only at the endpoints of creases. As specified earlier, only triangular and quadrilateral facets will be considered. Unlike the bar-hinge approach, facets are treated as 2D continua and the material properties can be directly used in the computation.

2.1. Membrane Deformation

The membrane deformation of the triangular and quadrilateral facets can be considered by any geometric nonlinear 3D T3 and Q4 membrane elements, respectively. Since ABAQUS does not have solely geometric nonlinear membrane element, its M3D3 T3 and M3D4 Q4 3D membrane elements for general nonlinearity are employed whilst the material is taken to be linear elastic and isotropic. In the two elements, membrane deformation is quantified by the in-plane logarithmic strain. Though logarithmic strain is unnecessarily complicated for small strain problems, M3D3 and M3D4 are adopted because ABAQUS does not display the user-defined element in its post-processor. The presence of the adjacent non-coplanar facets allows one to assume that the creases are straight due to the large membrane stiffness. The assumption implies the T3 facet cannot be bent and it is not necessary to consider its bending deformation. For the Q4 facet, the following subsection will derive a method to quantify the bending deformation under large displacement large rotation but small strain and small curvature assumption using a corotational consideration.

2.2. Bending Deformation of Quadrilateral Facet

Figure 2 shows the initial, corotated and deformed configurations of a quadrilateral facet. In the initial configuration, the element is flat whilst P and Q are the overlapping points along the straight lines 1-3 and 2-4, respectively. The deformed and corotated configurations are obtained from initial

configuration through respectively the displacement $\mathbf{U}$ and a rigid body displacement $\mathbf{U}^c$ defined with respect to the global coordinate (X,Y,Z). The location of node/point i (= 1, 2, 3, 4, P and Q) in the two configurations are denoted by i' and i^c. Since $\mathbf{U}^c$ is a rigid body displacement, 1^c-2^c-3^c-4^c is flat whilst P^c and Q^c remain overlapping. A local Cartesian coordinate system (x,y,z) is set up in the initial configuration and becomes (x^c,y^c,z^c) in the corotated configuration. Thus, the two sets of nodal coordinates (x_i,y_i) and (x_i^c, y_i^c) are identical. The deformed configuration can be obtained from the corotated configuration through the displacement $\mathbf{u} = \{u,v,w\}^T$ defined with respect to (x^c,y^c,z^c) of unit vectors ($\mathbf{e}_x^c$, $\mathbf{e}_y^c$, $\mathbf{e}_z^c$) defined with respect to (X,Y,Z), i.e.

$$\mathbf{U} = \mathbf{U}^c + [\mathbf{e}_x^c, \mathbf{e}_y^c, \mathbf{e}_z^c]^T \mathbf{u} \tag{1}$$

The rigid body displacement $\mathbf{U}^c$ is chosen such that it brings 1^c-2^c-3^c-4^c close to $1'$-$2'$-$3'$-$4'$ such that the small displacement assumption is applicable to $\mathbf{u}$ for deriving the strain and curvature. Its idea is similar to the approach for deriving curvatures in fabric materials (Liu and Sze 2009; Zhou and Sze 2012).
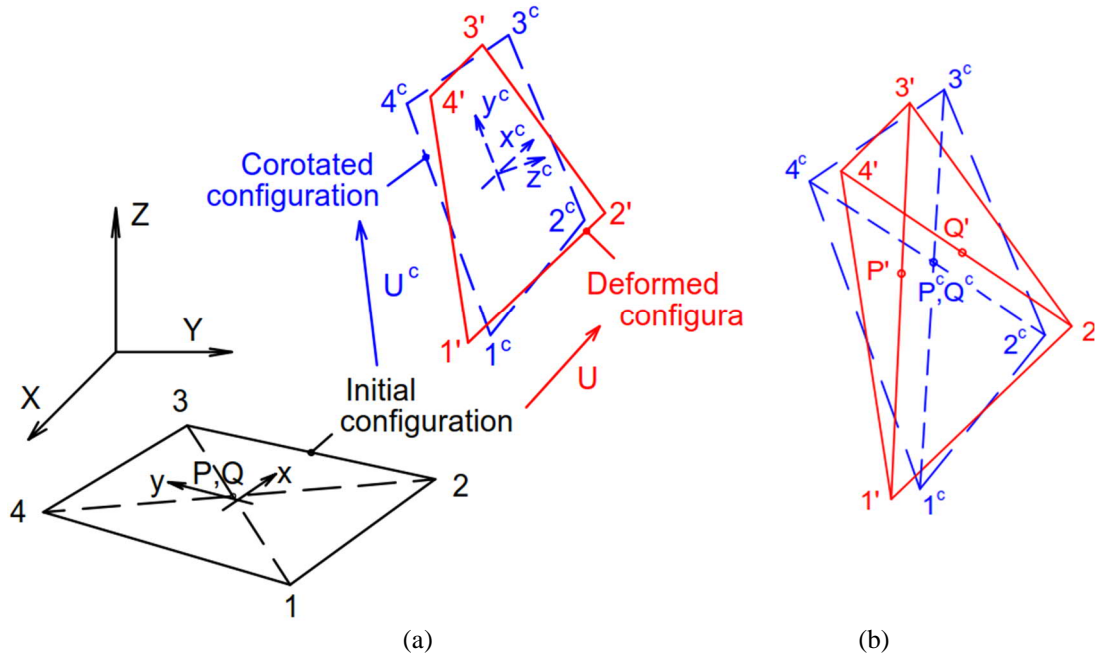

Figure 2 (a) Initial, corotated and deformed configurations of the Q4 bending element.
(b) P and Q are along the diagonals in the initial configuration.

The interpolated (x^c,y^c) and $\mathbf{u}$ in terms of the parametric coordinates of the element $\xi,\eta \in [-1,+1]$ can be expressed as

$$\begin{Bmatrix} x^c \\ y^c \end{Bmatrix} = \sum_{i=1}^{4} N_i \begin{Bmatrix} x_i^c \\ y_i^c \end{Bmatrix} = \sum_{i=1}^{4} N_i \begin{Bmatrix} x_i \\ y_i \end{Bmatrix} = \begin{Bmatrix} a_0 + a_1\xi + a_2\xi\eta + a_3\eta \\ b_0 + b_1\xi + b_2\xi\eta + b_3\eta \end{Bmatrix},$$

$$\mathbf{u} = \left\{ \begin{array}{c} u \\ v \\ w \end{array} \right\} = \sum_{i=1}^{4} N_i \mathbf{u}_i = \sum_{i=1}^{4} N_i \left\{ \begin{array}{c} u_i \\ v_i \\ w_i \end{array} \right\} \qquad (2\text{a,b})$$

where

$$\left[\begin{array}{c} N_1 \\ N_2 \\ N_3 \\ N_4 \end{array} \right] = \frac{1}{4} \left[\begin{array}{c} (1-\xi)(1-\eta) \\ (1+\xi)(1-\eta) \\ (1+\xi)(1+\eta) \\ (1-\xi)(1+\eta) \end{array} \right] , \quad \left[\begin{array}{cc} a_0 & b_0 \\ a_1 & b_1 \\ a_2 & b_2 \\ a_3 & b_3 \end{array} \right] = \frac{1}{4} \left[\begin{array}{cccc} +1 & +1 & +1 & +1 \\ -1 & +1 & +1 & -1 \\ +1 & -1 & +1 & -1 \\ -1 & -1 & +1 & +1 \end{array} \right] \left[\begin{array}{cc} x_1 & y_1 \\ x_2 & y_2 \\ x_3 & y_3 \\ x_4 & y_4 \end{array} \right] .$$

It can be checked that the deformed element edge, at $\xi = \pm 1$ or $\eta = \pm 1$, is linearly interpolated from the two edge end nodes. Hence, the straight crease assumption is always fulfilled by the element. From the interpolation in (2a), the chain rule of differentiation can be derived as

$$\frac{\partial}{\partial x^c} = \frac{1}{j} \left((b_2\xi + b_3) \frac{\partial}{\partial \xi} - (b_2\eta + b_1) \frac{\partial}{\partial \eta} \right), \frac{\partial}{\partial y^c} = \frac{1}{j} \left(-(a_2\xi + a_3) \frac{\partial}{\partial \xi} + (a_2\eta + a_1) \frac{\partial}{\partial \eta} \right) \qquad (3)$$

in which $j = \dfrac{\partial x^c}{\partial \xi} \dfrac{\partial y^c}{\partial \eta} - \dfrac{\partial x^c}{\partial \eta} \dfrac{\partial y^c}{\partial \xi} = j_0 + j_1\xi + j_2\eta$ is the Jacobian determinant and

$$j_0 = a_1 b_3 - a_3 b_1 \; , \; j_1 = a_1 b_2 - a_2 b_1 \; , \; j_2 = a_2 b_3 - a_3 b_2 .$$

The 3D Q4 element possesses 12 dofs and 6 rigid body modes. Hence, the element possesses 6 deformation modes among them 5 are membrane deformation modes. For a square element on the x^c-y^c-plane and with edges parallel to the x^c- or y^c-axis, the five membrane deformation modes are

$$\mathbf{u} = \left\{ \begin{array}{c} x^c \\ 0 \\ 0 \end{array} \right\} , \quad \mathbf{u} = \left\{ \begin{array}{c} 0 \\ y^c \\ 0 \end{array} \right\} , \quad \mathbf{u} = \left\{ \begin{array}{c} y^c \\ x^c \\ 0 \end{array} \right\} , \quad \mathbf{u} = \left\{ \begin{array}{c} x^c y^c \\ 0 \\ 0 \end{array} \right\} , \quad \mathbf{u} = \left\{ \begin{array}{c} 0 \\ x^c y^c \\ 0 \end{array} \right\} . \qquad (4)$$

The remaining deformation mode is a bending mode. By applying the differential operator to the interpolated w in (2b), the following curvature components can be worked out

$$\frac{\partial^2 w}{\partial^2 x^c} = -\frac{(b_2\xi + b_3)(b_2\eta + b_1)}{j^3} j_0 \Delta w \; , \; \frac{\partial^2 w}{\partial^2 y^c} = -\frac{(a_2\xi + a_3)(a_2\eta + a_1)}{j^3} j_0 \Delta w \; ,$$

$$2 \frac{\partial^2 w}{\partial x^c \partial y^c} = \frac{(a_1\xi + a_2\xi\eta + a_3\eta)b_2 + (b_1\xi + b_2\xi\eta + b_3\eta)a_2 + a_1 b_3 + a_3 b_1}{j^3} j_0 \Delta w \qquad (5)$$

where

$$\Delta w = \frac{j_0 + j_1 + j_2}{2 j_0} w_1 + \frac{-j_0 + j_1 - j_2}{2 j_0} w_2 + \frac{j_0 - j_1 - j_2}{2 j_0} w_3 + \frac{-j_0 - j_1 + j_2}{2 j_0} w_4 . \qquad (6)$$

Hence, the bending mode is featured by Δw. To stabilize the bending mode, it would be sufficient to evaluate the bending energy using one point quadrature which samples the curvature at $\xi = \eta = 0$. Effectively, one takes

$$\frac{\partial^2 w}{\partial^2 x^c} = \frac{-b_3 b_1}{j_0^2} \Delta w \; , \; \frac{\partial^2 w}{\partial^2 y^c} = \frac{-a_3 a_1}{j_0^2} \Delta w \; , \; 2 \frac{\partial^2 w}{\partial x^c \partial y^c} = \frac{a_1 b_3 + a_3 b_1}{j_0^2} \Delta w \; . \qquad (7)$$

For most papers, it is reasonable to assume isotropy. Thus, elastic energy of the Q4 bending element is

$$U_b = \frac{1}{2} D \int_{-1}^{+1}\int_{-1}^{+1} \left\{ \begin{array}{c} \partial^2 w/\partial^2 x^c \\ \partial^2 w/\partial^2 y^c \\ 2\partial^2 w/\partial x^c\partial y^c \end{array} \right\} \begin{bmatrix} 1 & v & 0 \\ v & 1 & 0 \\ 0 & 0 & (1-v)/2 \end{bmatrix} \left\{ \begin{array}{c} \partial^2 w/\partial^2 x^c \\ \partial^2 w/\partial^2 y^c \\ 2\partial^2 w/\partial x^c\partial y^c \end{array} \right\} j d\xi d\eta = \frac{D^e}{2}(\Delta w)^2 \quad (8)$$

where $D = Eh^3/(1-v^2)/12$ is the bending rigidity, E is the elastic modulus E, v is the Poisson's ratio, h is the paper thickness and $D^e = 2D[2(b_3b_1 + a_3a_1)^2 + (1-v)j_0^2]/j_0^3$. More complicated material models can also be considered.

A physical interpretation of Δw in (7) is then identified by referring to points P^c and Q^c in Figure 2(b). As a point of remark, P^c is along 1^c-3^c, Q^c is along 2^c-4^c and the two points are intersecting. It can be solved that

$$\left\{ \begin{array}{c} x_P^c \\ y_P^c \end{array} \right\} = \left\{ \begin{array}{c} x_Q^c \\ y_Q^c \end{array} \right\} = \left\{ \begin{array}{c} x_P \\ y_P \end{array} \right\} = \left\{ \begin{array}{c} x_Q \\ y_Q \end{array} \right\} = \frac{1}{j_0} \left\{ \begin{array}{c} a_0 j_0 - a_1 j_1 - a_3 j_2 \\ b_0 j_0 - b_1 j_1 - b_3 j_2 \end{array} \right\} . \quad (9)$$

Now, **u** of P^c is linearly interpolated from those at 1^c and 3^c whilst the displacement of Q^c is linearly interpolated from those of 2^c and 4^c. Thus,

$$\mathbf{u}_P - \mathbf{u}_Q = \left\{ \begin{array}{c} u_P - u_Q \\ v_P - v_Q \\ w_P - w_Q \end{array} \right\} = \frac{l_{1P}\mathbf{u}_3 + l_{P3}\mathbf{u}_1}{l_{13}} - \frac{l_{2Q}\mathbf{u}_4 + l_{Q4}\mathbf{u}_2}{l_{24}} = M_1\mathbf{u}_1 + M_2\mathbf{u}_2 + M_3\mathbf{u}_3 + M_4\mathbf{u}_4 \quad (10)$$

where $l_{ij} = \sqrt{(x_i - x_j)^2 + (y_i - y_j)^2}$ and $M_1 = \frac{l_{P3}}{l_{13}}, M_2 = -\frac{l_{Q4}}{l_{24}}, M_3 = \frac{l_{1P}}{l_{13}}, M_4 = -\frac{l_{2Q}}{l_{24}}$. Recalling

$$(\frac{l_{1P}}{l_{13}}, \frac{l_{P3}}{l_{13}}) = (\frac{x_1 - x_P}{x_1 - x_3}, \frac{x_P - x_3}{x_1 - x_3}) \text{ for } x_1 \neq x_3 \ , \ (\frac{l_{1P}}{l_{13}}, \frac{l_{P3}}{l_{13}}) = (\frac{y_1 - y_P}{y_1 - y_3}, \frac{y_P - y_3}{y_1 - y_3}) \text{ for } y_1 \neq y_3 ,$$

$$(\frac{l_{2Q}}{l_{24}}, \frac{l_{Q4}}{l_{24}}) = (\frac{x_2 - x_Q}{x_2 - x_4}, \frac{x_Q - x_4}{x_2 - x_4}) \text{ for } x_2 \neq x_4 \text{ and } (\frac{l_{2Q}}{l_{24}}, \frac{l_{Q4}}{l_{24}}) = (\frac{y_2 - y_Q}{y_2 - y_4}, \frac{y_Q - y_4}{y_2 - y_4}) \text{ for } y_2 \neq y_4 ,$$

further manipulations can show that

$$w_P - w_Q = \Delta w \quad (11)$$

which provides a physical interpretation of Δw defined in (6). For thin beam/plate under small displacement, it is well-known that the out-of-plane displacement will dominate in general. A simple illustration is given in Figure 3. Unless the tip force is applied axially to the cantilever ($\alpha = 0$), otherwise the out-of-plane displacement would be far larger than the in-plane displacement for thin beams. Thus, **u** would be dominated by w and a good approximation to (11) after taking the magnitude is

$$|\Delta w| = |w_P - w_Q| = |\mathbf{u}_P - \mathbf{u}_Q| . \quad (12)$$

$$\frac{w_{tip}}{u_{tip}} = \frac{\dfrac{FL^3 \sin\alpha}{3EI}}{\dfrac{FL\cos\alpha}{AE}} = \frac{AL^2}{3I}\tan\alpha$$
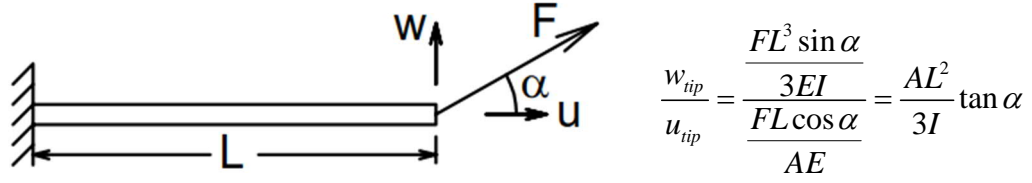
Fig. 3 A cantilever with an inclined tip force acting and the ratio of its out-of-plane to in-plane deflection at the tip. For thin bean $L^2 \gg I/A$.

Applying the same method of interpolation of **u** in the corotated configuration, see (10), to **U** in the initial configuration, one obtains

$$\mathbf{U}_P - \mathbf{U}_Q = \frac{l_{1P}\mathbf{U}_3 + l_{P3}\mathbf{U}_1}{l_{13}} - \frac{l_{2Q}\mathbf{U}_4 + l_{Q4}\mathbf{U}_2}{l_{24}} = [M_1\mathbf{I}_3, M_2\mathbf{I}_3, M_3\mathbf{I}_3, M_4\mathbf{I}_3]\begin{Bmatrix}\mathbf{U}_1 \\ \vdots \\ \mathbf{U}_4\end{Bmatrix} \tag{13}$$

By invoking (1),

$$\mathbf{U}_P - \mathbf{U}_Q = (\mathbf{U}_P^c + [\mathbf{e}_x, \mathbf{e}_y, \mathbf{e}_z]^T \mathbf{u}_P) - (\mathbf{U}_Q^c + [\mathbf{e}_x, \mathbf{e}_y, \mathbf{e}_z]^T \mathbf{u}_Q) = [\mathbf{e}_x, \mathbf{e}_y, \mathbf{e}_z]^T(\mathbf{u}_P - \mathbf{u}_Q) \tag{14}$$

in which $\mathbf{U}_P^c$ and $\mathbf{U}_Q^c$ cancel each other because P^c and Q^c are overlapping. By incorporating (12), (13), (13) and the property of the orthogonal matrix $[\mathbf{e}_x^c, \mathbf{e}_y^c, \mathbf{e}_z^c]$, (8) can be expressed as

$$U_b = \frac{D^e}{2}(\Delta w)^2 = \frac{D^e}{2}(\mathbf{u}_P - \mathbf{u}_Q)^T(\mathbf{u}_P - \mathbf{u}_Q) = \frac{D^e}{2}(\mathbf{U}_P - \mathbf{U}_Q)^T(\mathbf{U}_P - \mathbf{U}_Q)$$

$$= \frac{1}{2}\begin{Bmatrix}\mathbf{U}_1 \\ \mathbf{U}_2 \\ \mathbf{U}_3 \\ \mathbf{U}_4\end{Bmatrix}^T (D^e\begin{bmatrix} M_1M_1\mathbf{I}_3 & M_1M_2\mathbf{I}_3 & M_1M_3\mathbf{I}_3 & M_1M_4\mathbf{I}_3 \\ M_2M_1\mathbf{I}_3 & M_2M_2\mathbf{I}_3 & M_2M_3\mathbf{I}_3 & M_2M_4\mathbf{I}_3 \\ M_3M_1\mathbf{I}_3 & M_3M_2\mathbf{I}_3 & M_3M_3\mathbf{I}_3 & M_3M_4\mathbf{I}_3 \\ M_4M_1\mathbf{I}_3 & M_4M_2\mathbf{I}_3 & M_4M_3\mathbf{I}_3 & M_4M_4\mathbf{I}_3 \end{bmatrix})\begin{Bmatrix}\mathbf{U}_1 \\ \mathbf{U}_2 \\ \mathbf{U}_3 \\ \mathbf{U}_4\end{Bmatrix} \tag{15}$$

where the matrix inside the braces is the tangential stiffness matrix of the Q4 bending element. Unlike most tangential stiffness matrix used in nonlinear analysis, the present one is a constant matrix which does not need to be updated in the iterative solution procedure and is in line with that for quantifying the bending energy in fabrics in (Liu and Sze 2009; Zhou and Sze 2012). Unlike the conventional corotational formulation, the choice of the corotational configuration is purely notional here as the above energy is independent of $\mathbf{U}^c$.

3. CREASE MODELLING

Inter-facet edges are creases which are often modelled as spring-loaded hinges. Previous determinations of the dihedral angle involve using simultaneous dot and cross products of selected vectors (Liu and Paulino 2017; Schenk and Guest 2011; Bekker 1996). Alternatively, the *arctan2* function is used at the

expense of using two arguments in the function (Gillman et al. 2018). Based on the large-displacement but small-strain and small-curvature assumption, an approximate method is here devised that can considerably simplify the fold angle, a complement of dihedral angle, and its derivatives with respect to the nodal displacement.

Left-hand side of Figure 4 shows the initial crease 1-3 between the flat facets 1-2-3 and 1-3-4-E. Among nodes 4 and E, the one closer to the mid-point of 1-3, i.e. node 4, is used to determine the initial fold angle θ_o which is normally zero. P and Q are points along 1-3 such that P-4 and Q-2 are perpendicular to 1-3. Thus, the position vectors $\mathbf{X}_P$ and $\mathbf{X}_Q$ can be expressed as:

$$\mathbf{X}_P = \mathbf{X}_1 + s_P(\mathbf{X}_3 - \mathbf{X}_1) \ , \ \mathbf{X}_Q = \mathbf{X}_1 + s_Q(\mathbf{X}_3 - \mathbf{X}_1) \tag{16}$$

where the non-dimensional coordinates s_P and s_Q can be solved from the orthogonality relations $(\mathbf{X}_3 - \mathbf{X}_1) \cdot (\mathbf{X}_4 - \mathbf{X}_P) = 0$ and $(\mathbf{X}_3 - \mathbf{X}_1) \cdot (\mathbf{X}_2 - \mathbf{X}_Q) = 0$ to be

$$s_P = \frac{(\mathbf{X}_3 - \mathbf{X}_1) \cdot (\mathbf{X}_4 - \mathbf{X}_1)}{|\mathbf{X}_3 - \mathbf{X}_1|^2} \ , \ s_Q = \frac{(\mathbf{X}_3 - \mathbf{X}_1) \cdot (\mathbf{X}_2 - \mathbf{X}_1)}{|\mathbf{X}_3 - \mathbf{X}_1|^2} . \tag{17}$$

Thus,

$$\underline{P4} = \mathbf{X}_4 - \mathbf{X}_P = \mathbf{X}_4 - (1 - s_P)\mathbf{X}_1 - s_P\mathbf{X}_3 \ , \quad \underline{Q2} = \mathbf{X}_2 - \mathbf{X}_Q = \mathbf{X}_2 - (1 - s_Q)\mathbf{X}_1 - s_Q\mathbf{X}_3 . \tag{18}$$

In the equation, $\underline{IJ}$ denotes the vector from I to J where $I, J = 1, 2, 3, 4, P$ and Q. The initial fold angle θ_o can be obtained as

$$\cos\theta_o = -\frac{\underline{P4} \cdot \underline{Q2}}{|\underline{P4}| \cdot |\underline{Q2}|} \quad \text{and} \quad \theta_o = \begin{cases} \cos^{-1}(-\dfrac{\underline{P4} \cdot \underline{Q2}}{|\underline{P4}| \cdot |\underline{Q2}|}) & \text{for } (\underline{P4} \times \underline{Q2}) \cdot (\mathbf{X}_3 - \mathbf{X}_1) > 0 \\ -\cos^{-1}(-\dfrac{\underline{P4} \cdot \underline{Q2}}{|\underline{P4}| \cdot |\underline{Q2}|}) & \text{otherwise} \end{cases} \tag{19}$$

in which $\cos^{-1}$ returns the principal value of the angle between 0 and π. It is trivial that the fold angle and dihedral angle are complementary, i.e. their sum is π. A similar way of computing the dihedral angle can be noted in (Bekker 1996).
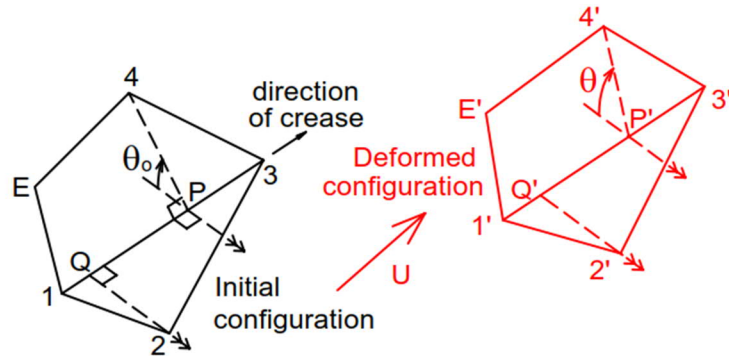

Fig. 4 The crease 1-3 between the facets 1-2-3 and 1-3-4-E in its initial and deformed configurations. The fold angle changes from θ_o to θ.

After displacement $\mathbf{U}$, J moves to J' whose position vector is $\mathbf{X}_{J'} = \mathbf{X}_J + \mathbf{U}_J$. Following (18), the displaced $P4$ and $Q2$ become

$$\mathbf{p} = \underline{P'4'} = \underline{P4} + \mathbf{U}_4 - (1 - s_P)\mathbf{U}_1 - s_P\mathbf{U}_3 \ , \quad \mathbf{q} = \underline{Q'2'} = \underline{Q2} + \mathbf{U}_2 - (1 - s_Q)\mathbf{U}_1 - s_Q\mathbf{U}_3 . \tag{20}$$

The deformation due to crease folding often dominates the overall deformation to which the facet membrane and bending deformations also contribute. Under the large-displacement but small-strain and small-curvature assumption for the facet, close approximations to the fold angle θ and the unit vector $\mathbf{n}$ along $\mathbf{p} \times \mathbf{q}$ can be taken to be

$$\cos\theta = -\frac{\mathbf{p} \cdot \mathbf{q}}{pq} \quad \text{and} \quad \theta = \begin{cases} \cos^{-1}(-\dfrac{\mathbf{p} \cdot \mathbf{q}}{pq}) & \text{for } (\mathbf{p} \times \mathbf{q}) \cdot \underline{1'3'} > 0 \\[2ex] -\cos^{-1}(-\dfrac{\mathbf{p} \cdot \mathbf{q}}{pq}) & \text{otherwise} \end{cases} \tag{21a,b}$$

and

$$\mathbf{n} = \frac{\mathbf{X}_{3'} - \mathbf{X}_{1'}}{|\mathbf{X}_{3'} - \mathbf{X}_{1'}|} = \frac{\mathbf{X}_3 + \mathbf{U}_3 - \mathbf{X}_1 - \mathbf{U}_1}{|\mathbf{X}_3 + \mathbf{U}_3 - \mathbf{X}_1 - \mathbf{U}_1|} . \tag{22}$$

where $p = |\mathbf{p}|$ and $q = |\mathbf{q}|$. By invoking the relations in (20), derivative in (21a) with respect to $\mathbf{U}_C$ is

$$\frac{\partial\theta}{\partial\mathbf{U}_4} = \frac{1}{\sin\theta}(\frac{\mathbf{q}}{pq} - \frac{\mathbf{p} \cdot \mathbf{q}}{p^2 q}\frac{\partial p}{\partial\mathbf{U}_4}) = -\frac{(\mathbf{p} \cdot \mathbf{q})\mathbf{p} - (\mathbf{p} \cdot \mathbf{p})\mathbf{q}}{p^3 q \sin\theta} . \tag{23}$$

By substituting $\mathbf{a} = \mathbf{b} = \mathbf{p}$ and $\mathbf{c} = \mathbf{q}$ substituted into the identity $\mathbf{a} \times (\mathbf{b} \times \mathbf{c}) = (\mathbf{a} \cdot \mathbf{c})\mathbf{b} - (\mathbf{a} \cdot \mathbf{b})\mathbf{c}$, one gets $\mathbf{p} \times (\mathbf{p} \times \mathbf{q}) = (\mathbf{p} \cdot \mathbf{q})\mathbf{p} - (\mathbf{p} \cdot \mathbf{p})\mathbf{q}$ and

$$\frac{\partial\theta}{\partial\mathbf{U}_4} = -\frac{\mathbf{p} \times (\mathbf{p} \times \mathbf{q})}{p^3 q \sin\theta} = -\frac{\mathbf{p}}{p^2} \times (\frac{\mathbf{p} \times \mathbf{q}}{pq \sin\theta}) = -\frac{\mathbf{p} \times \mathbf{n}}{p^2} . \tag{24}$$

Similarly, one can derive

$$\frac{\partial\theta}{\partial\mathbf{U}_2} = -\frac{\mathbf{n} \times \mathbf{q}}{q^2} . \tag{25}$$

By invoking (20), it can be shown that

$$\frac{\partial\theta}{\partial\mathbf{U}_1} = -(1 - s_P)\frac{\partial\theta}{\partial\mathbf{U}_4} - (1 - s_Q)\frac{\partial\theta}{\partial\mathbf{U}_2} \ , \quad \frac{\partial\theta}{\partial\mathbf{U}_3} = -s_P\frac{\partial\theta}{\partial\mathbf{U}_4} - s_Q\frac{\partial\theta}{\partial\mathbf{U}_2} . \tag{26}$$

From (22), (24), (25) and (26), all the first order derivatives of θ with respect to the nodal displacement are determined.

Before proceeding to the second order derivatives of θ, the following identities for any arbitrary vectors $\mathbf{a} = \{a_i\}$ and $\mathbf{b} = \{b_i\}$ are recalled:

$$\mathbf{a} \times \mathbf{b} = [\mathbf{a}]_\times \mathbf{b} \ , \quad \mathbf{a} \otimes (\mathbf{a} \times \mathbf{b}) - (\mathbf{a} \times \mathbf{b}) \otimes \mathbf{a} = (\mathbf{a} \cdot \mathbf{a})[\mathbf{b}]_\times - (\mathbf{a} \cdot \mathbf{b})[\mathbf{a}]_\times \tag{27a,b}$$

where

$$[\mathbf{c}]_\times = \begin{bmatrix} 0 & -c_3 & c_2 \\ c_3 & 0 & -c_1 \\ -c_2 & c_1 & 0 \end{bmatrix} \text{ for any vector } \mathbf{c} = \{c_i\} \text{ and } \mathbf{a} \otimes \mathbf{b} = [a_i b_j] .$$

By taking $\mathbf{a} = \mathbf{p}$ and $\mathbf{b} = \mathbf{n}$, and invoking the approximation $\mathbf{p} \cdot \mathbf{n} = 0$, (27b) becomes

$$\mathbf{p} \otimes (\mathbf{p} \times \mathbf{n}) - (\mathbf{p} \times \mathbf{n}) \otimes \mathbf{p} = p^2[\mathbf{n}]_\times \ . \tag{28}$$

Noting that $\mathbf{n}$ in (22) is independent of $\mathbf{U}_2$ and $\mathbf{U}_4$, (28) leads to

$$\frac{\partial^2 \theta}{\partial \mathbf{U}_4^T \partial \mathbf{U}_4} = \frac{[\mathbf{n}]_\times}{p^2} + \frac{2}{p^4}(\mathbf{p} \times \mathbf{n}) \otimes \mathbf{p} = \frac{1}{p^4}[(\mathbf{p} \times \mathbf{n}) \otimes \mathbf{p} + \mathbf{p} \otimes (\mathbf{p} \times \mathbf{n})] \tag{29}$$

By invoking $\mathbf{q} \cdot \mathbf{n} = 0$, one can similarly obtain

$$\frac{\partial^2 \theta}{\partial \mathbf{U}_2 \partial \mathbf{U}_2} = -\frac{[\mathbf{n}]_\times}{q^2} - \frac{2}{q^4}(\mathbf{q} \times \mathbf{n}) \otimes \mathbf{q} = -\frac{1}{q^4}[(\mathbf{q} \times \mathbf{n}) \otimes \mathbf{q} + \mathbf{q} \otimes (\mathbf{q} \times \mathbf{n})] \tag{30}$$

By recalling (20), other second-order derivatives of θ with respect to the nodal displacement can be expressed as

$$\frac{\partial^2 \theta}{\partial \mathbf{U}_4^T \partial \mathbf{U}_2} = \mathbf{0} \ , \ \frac{\partial^2 \theta}{\partial \mathbf{U}_4^T \partial \mathbf{U}_1} = -(1 - s_P)\frac{\partial^2 \theta}{\partial \mathbf{U}_4^T \partial \mathbf{U}_4} \ , \ \frac{\partial^2 \theta}{\partial \mathbf{U}_4^T \partial \mathbf{U}_3} = -s_P \frac{\partial^2 \theta}{\partial \mathbf{U}_4^T \partial \mathbf{U}_4} \ ,$$

$$\frac{\partial^2 \theta}{\partial \mathbf{U}_2^T \partial \mathbf{U}_1} = -(1 - s_Q)\frac{\partial^2 \theta}{\partial \mathbf{U}_2^T \partial \mathbf{U}_2} \ , \ \frac{\partial^2 \theta}{\partial \mathbf{U}_2^T \partial \mathbf{U}_3} = -s_Q \frac{\partial^2 \theta}{\partial \mathbf{U}_2^T \partial \mathbf{U}_2} \ ,$$

$$\frac{\partial^2 \theta}{\partial \mathbf{U}_1^T \partial \mathbf{U}_1} = (1 - s_P)^2 \frac{\partial^2 \theta}{\partial \mathbf{U}_4^T \partial \mathbf{U}_4} + (1 - s_Q)^2 \frac{\partial^2 \theta}{\partial \mathbf{U}_2^T \partial \mathbf{U}_2} \ ,$$

$$\frac{\partial^2 \theta}{\partial \mathbf{U}_1^T \partial \mathbf{U}_3} = s_P(1 - s_P)\frac{\partial^2 \theta}{\partial \mathbf{U}_4^T \partial \mathbf{U}_4} + s_Q(1 - s_Q)\frac{\partial^2 \theta}{\partial \mathbf{U}_2^T \partial \mathbf{U}_2} \ ,$$

$$\frac{\partial^2 \theta}{\partial \mathbf{U}_3^T \partial \mathbf{U}_3} = s_P^2 \frac{\partial^2 \theta}{\partial \mathbf{U}_4^T \partial \mathbf{U}_4} + s_Q^2 \frac{\partial^2 \theta}{\partial \mathbf{U}_2^T \partial \mathbf{U}_2} \ . \tag{31}$$

The elastic energy of the crease can be assumed to be

$$U_c = \frac{kl}{2}(\theta - \theta_o)^2 \tag{32}$$

where k is the fold stiffness per unit length of the crease and $l = |\mathbf{X}_3 - \mathbf{X}_1|$ is the initial length of the crease. The internal force and tangent stiffness matrix are

$$\mathbf{f}_c = \begin{Bmatrix} \mathbf{f}_1 \\ \mathbf{f}_2 \\ \mathbf{f}_3 \\ \mathbf{f}_4 \end{Bmatrix} \quad \text{and} \quad \mathbf{k}_c = \begin{bmatrix} \mathbf{k}_{11} & \mathbf{k}_{12} & \mathbf{k}_{13} & \mathbf{k}_{14} \\ & \mathbf{k}_{22} & \mathbf{k}_{23} & \mathbf{k}_{24} \\ & & \mathbf{k}_{33} & \mathbf{k}_{34} \\ sym. & & & \mathbf{k}_{44} \end{bmatrix} \tag{33}$$

in which

$$\mathbf{f}_i = \frac{\partial U_c}{\partial \mathbf{U}_i} = kl(\theta - \theta_o)\frac{\partial \theta}{\partial \mathbf{U}_i} \quad \text{and} \quad \mathbf{k}_{ij} = \frac{\partial^2 U}{\partial \mathbf{U}_i^T \partial \mathbf{U}_j} = kl\frac{\partial \theta}{\partial \mathbf{U}_i} \otimes \frac{\partial \theta}{\partial \mathbf{U}_j} + kl(\theta - \theta_o)\frac{\partial^2 \theta}{\partial \mathbf{U}_i^T \partial \mathbf{U}_j} \tag{34}$$

in which derivatives of θ has been derived in (24) to (26) and (29) to (31). As the crease involves nodes 1, 2, 3 and 4, it would be termed and implemented as a 4-node crease element. It is trivial that the crease element is equally applicable to model elastic hinges.

4. PRESCRIBING FOLD ANGLES

In origami simulation, it is sometimes more convenient to prescribe the fold angle θ to its rest angle θ_{rest} which defines the zero energy configuration of the crease (Ghassaei et al. 2018). Furthermore, it is often necessary to apply the prescribed θ_{rest} incrementally to minimize divergence in the nonlinear solution procedure. To effect $\theta = \theta_{rest}$ incrementally, the elastic energy of the crease can be modified to

$$U_c = \frac{kl}{2}(\theta - \bar{\theta})^2 \tag{35}$$

where $\bar{\theta} = (1-t)\theta_o + t\theta_{rest}$ and t varies from 0 (start of the analysis step) to 1 (end of the analysis step). The related element internal force vector and tangential stiffness matrix can be obtained by replacing θ_o with $\bar{\theta}$ in (34). In reality, multiple creases would be prescribed with their rest angles and θs may only be approximately equal to $\bar{\theta}$ s in the converged solution. For simplicity, prescription of the rest angle as the means to deform an origami would be termed as the rest angle loading.

5. NUMERICAL EXAMPLES

The Q4 bending element and the 4-node crease element are incorporated into ABAQUS thru its user-defined element or UEL subroutines. They are co-used with ABAQUS's 3D membrane elements M3D4 and M3D3 to realize the origami simulations. Modification of the subroutine is needed for specifying the rest-angle loading. In the automatic time increment feature of ABAQUS, the prescribed loading is applied incrementally as a function of time t which varies from 0 (start of the analysis step) to 1 (end of the analysis step). For each increment, the Newton-Raphson method is used to refine the iterative solution until the default convergence criteria, i.e. the 0.5% force tolerance and the 1% displacement tolerance, are met simultaneously. Unless specified otherwise, the default automatic time increment is employed with the initial and minimum time increment set to be 1 and 10^{-5}, respectively. In the automatic time increment process, if the solution cannot converge within 16 iterations, the scheme abandons the increment and starts again with the time increment reduced to one-quarter of the present value. If the solution still fails to converge, the scheme reduces the increment again. If the time increment becomes smaller than the minimum or the solution fails after 5 reductions, the analysis will be aborted. On the other hand, the time increment increases by 50% if the last two converged solutions are both attained within 5 iterations. The computation is conducted in the same laptop PC, with Intel(R) Core(TM) i9-9880H CPU (8 cores, 2.30 GHz) and 64 GB RAM, used to produce the results in Fig. 1 and Table 1.

In the description of the examples and the ABAQUS calculations, SI units are employed and would not be further specified. The properties of paperboard $E = 3 \times 10^9$, $\nu = 0.3$ and $h = 0.27 \times 10^{-3}$ are adopted (Filipov et al. 2017; Schulgasser 1983). The fold stiffness per unit crease length is taken to be proportional to the bending rigidity, i.e., $k = D/L^*$ where L^* is a length scaling factor (Lechenault et al. 2014). For paperboards, L^* varies typically from 1.6×10^{-3} to 133×10^{-3} m, see Table 1 of reference

(Filipov et al. 2017). In Sections 5.1, 5.2, 5.3 and 5.6, $k = 0.1$ is used which corresponds to $L^* = 54 \times 10^{-3}$. The video animation files for the examples are provided as Online Resources. They are prepared by the post-processor of ABAQUS with at least 60 time increments to enhance the visual smoothness.

5.1. Elastic Hinge

This example considers two identical panels connected by an elastic hinge and aims at illustrating the efficacy of the proposed crease element. It also serves to compare the convergence of different elements used to model the panels. The dimensions of the panels are: $L = 2$, $W = 1$ and $H = 0.05$. Practically, no strain will be induced in the panels. The nonlinearity of the problem mainly comes from the large displacement and rotation experienced by the elements. Here, four modelling methods are considered.

In the first method of modelling, the panels are modelled by ABAQUS's SC8R solid-shell element model which possesses no rotation dof. Eight elements are employed as shown in Fig. 5. B_1 to B_5 are pinned. C_1 and C_2 are restrained from moving along the X-direction. An elastic hinge is realized by having four nodes along A_1A_3 common to the two panels. The crease element $A_1A_2A_3A_4$ with initial fold angle $\theta_o = \pi$, see Fig. 5(a), provides the elastic effect to the hinge. A rest angle loading with $\theta_{rest} = 0$ is applied to unfold the panels. An intermediate configuration at $\theta \approx 2\pi/3$ and the final configuration at $\theta = 0$ are shown in Fig. 5(b) and 5(c), respectively. The animation video is given in Online Resource 1.
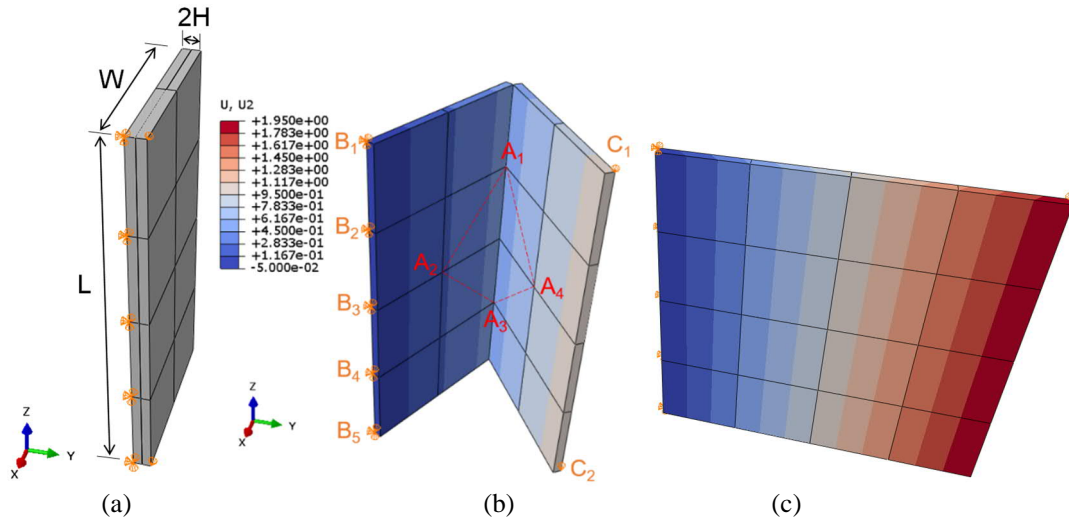

Fig. 5 Two panels connected by an elastic hinge. (a) The initial, (b) an intermediate and (c) the final configurations predicted by the 8-node solid-shell element model SC8R. The crease element $A_1A_2A_3A_4$ is defined using nodes on the faces of the two panels.

In the second method of modelling, A_2 and A_4 that define the crease element are then changed to nodes on the side edges of the panels, See Fig. 6. In other words, the crease element is initially flat ($\theta_o = 0$) and fully folded in the final configuration ($\theta_{rest} = \pi$). The animation video is given in Online Resource 2.
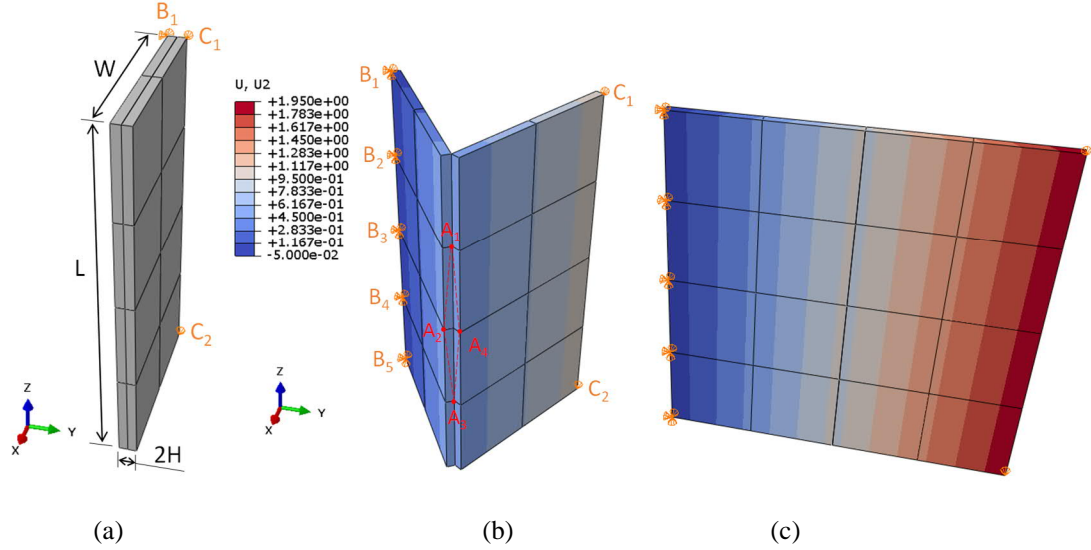
(a)   (b)   (c)

Fig. 6 Two panels connected by an elastic hinge. (a) The initial, (b) an intermediate and (c) the final configurations predicted by the 8-node solid-shell element model SC8R. The crease element $A_1A_2A_3A_4$ is defined using nodes on the side edges of the two panels.
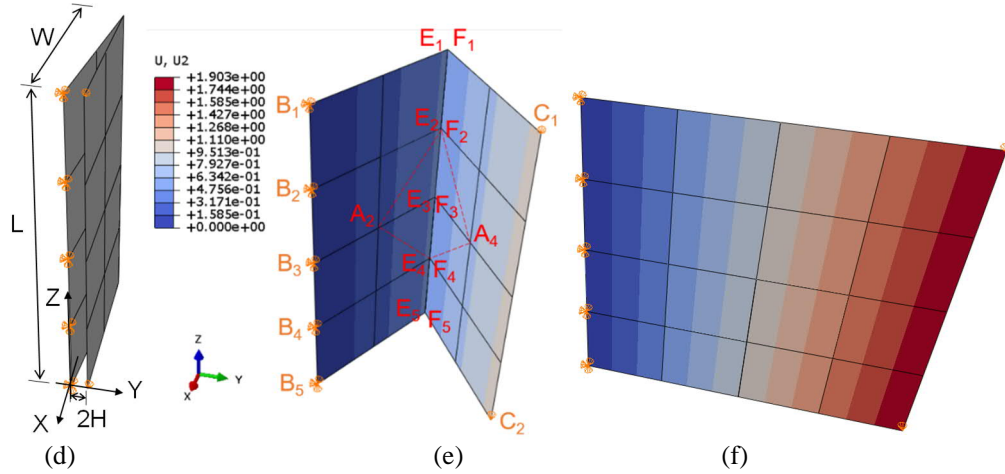

(d)   (e)   (f)

Fig.7 Two panels connected by an elastic hinge. (a) The initial, (b) an intermediate and (c) the final configurations predicted by the 4-node shell element model S4R.

In the third method of modelling, the S4R shell element model in ABAQUS is employed, see Fig. 7. The element possesses 4-node on the mid-surface of the plate/shell and each node has 3 translational and 3 rotational dofs. The boundary conditions prescribed to B_is and C_is are the same as those in SC8R. To avoid coupling the rotational dofs of the elements modelling the two panels, the two panels are created separately. The translational dofs of E_is and F_is are then tied by using the Multi-Point Constraint of PIN type in ABAQUS so that E_is and F_is share the same translational dofs. The crease element $E_2A_2E_4A_4$ with initial fold angle $\theta_o = \pi - 0.1$ is defined to provide the elastic effect to the hinge between the two panels. It should be remarked that the more natural setting $\theta_o = \pi$ is not used because it would cause all B_is and C_is lying on the same vertical line. The two fully folded panels can spin freely about the vertical line leading to the singular of the initial global stiffness matrix. Again, rest angle loading with $\theta_{rest} = 0$ is employed to unfold the panels. After the first few time increments, the time increments

15

of ABAQUS remain to be ~0.0014 throughout the simulation, see Table 2. An intermediate configuration $\theta \approx 2\pi/3$ and the final configuration are shown in Fig. 7(b) and 7(c), respectively. The animation video is given in Online Resource 3.

In the fourth method of modelling, the M3D4 3D membrane element model in ABAQUS, the Q4 bending element and crease elements are employed. The initial mesh is same as the one shown in Fig.7a whilst the two panels share the same nodes at the elastic hinge. In other words, nodes E_is and F_is in Fig.7b are identical and they need not be separately defined. Again, $E_2A_2E_4A_4$ is the crease element providing the elastic hinge effect. For 20 common element edges shared by adjacent elements within each panel, crease elements with a large stiffness ($k = 1000$) are defined to maintain the coplanarity of the panels. The predicted configurations are identical to those of the S4R shell element model in Fig. 7. The animation video is given in Online Resource 4.

The numbers of time increment and the CPU time consumed by the four methods of modelling are summarized in Table 2. The result echoes that the discussion in Section 1 on the relative convergence of the elements with and without rotational dofs. S4R shell element model consumes far more computing resource than the SC8R solid-shell element model which, in turn, is less computationally efficient than using the membrane element and the developed elements.

Table 2. Numbers of time increments and CPU times consumed in the elastic hinge problem.

Method of Modelling	First way	Second way	Third way	Fourth way
Elements used to model the two panels	SC8R	SC8R	S4R	M3D4, the developed Q4 bending and crease elements
No. of time increments	31	44	674	22
CPU time	1.9 sec	2.5 sec	41.6 sec	1.7 sec

5.2. Simple Pop-up Kirigami

This example considers the simple pop-up kirigami shown in Fig. 8. The kirigami is made from a square paper with two straight cuts B_2B_4 and C_2C_4. Initially, the paper is flat, i.e., $\theta_o = 0$ for all creases. Nodes B_0 and B_3 are at the two sides of B_2B_4 whilst nodes C_0 and C_3 are at the two sides of C_2C_4. Nodes B_1, B_2, C_1 and C_2 are fixed. Both the displacement and rest angle loading are prescribed to pop up the kirigami. Same as the last example, strain inside the facets is negligible and the nonlinearity comes from the large displacement and rotation experienced by the elements. It can also be considered by solid-shell element readily at the expense of high computational cost.

For the displacement loading, the applied displacements are listed in Table 3. ABAQUS takes 18 increments and 1.4 seconds of CPU time to complete the computation. The final configuration is shown in Fig. 8(b). The animation video is given in Online Resource 5. For the rest angle loading, the following rest fold angles are prescribed:

$$\theta_{rest} = \begin{cases} -\pi/2 & \text{for crease } B_0C_0 \\ \pi/2 & \text{for creases } B_2C_2, B_4C_4, A_3B_3 \text{ and } C_3D_3 \\ 0 & \text{for other creases} \end{cases} \quad . \tag{36}$$

16

ABAQUS takes 8 increments and 0.8 seconds of CPU time to complete the computation. The final folded form is graphically indistinguishable from Figure 8(b). The animation video is given in Online Resource 6.

Table 3 Displacement loading conditions for the pop-up kirigami, see Fig. 8.

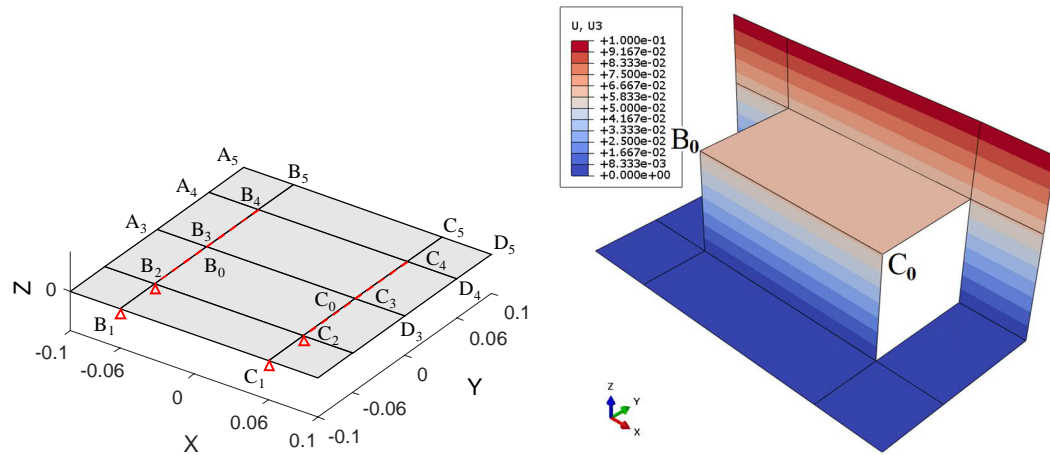| Nodes	A_3, B_3, C_3, D_3	B_0, C_0	A_5, B_5, C_5, D_5
Prescribed W	0	0.06	0.1

Fig. 8 (a) The initial configuration of a simple pop-up kirigami. B_0 and B_3 are at the two sides of the cut B_2B_4, C_0 and C_3 are at the two sides of the cut C_2C_4. (b) The final configuration.

5.3. Crane

As the crane is a symbol of happiness and eternal youth in most Asian countries, it is probably the most popular origami. Crane folding is considered in this example (Ghassaei et al. 2018). Fig. 9(a) shows the crease pattern which consists of triangular and quadrilateral facets. The zero displacement boundary conditions (i) $U = 0$ for A_1, (ii) $V = 0$ for A_1 and A_2, (iii) $W = 0$ for A_2, A_3 and A_4 are prescribed to prevent the rigid body movement of the origami. Same as the last example, both displacement and rest angle loadings are employed to deform the flat piece of paper in Fig. 9(a), i.e. $\theta_o = 0$, into the final folded form in Fig. 9(b).
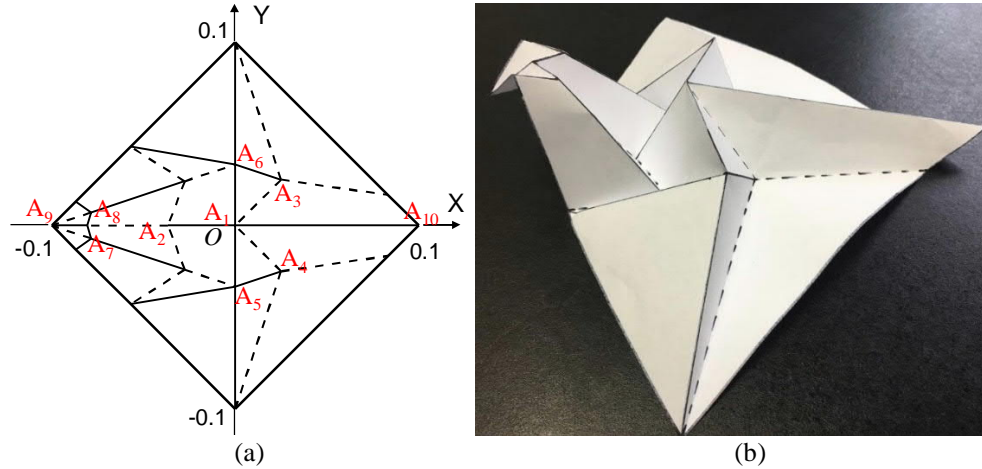
Fig. 9 Crane. (a) The crease pattern where the valley folds ($\theta_{rest} > 0$) and mountain folds ($\theta_{rest} < 0$) are indicated by chained and solid lines, respectively. (b) A paper model of the folded form.

In the displacement loading, several nodes are prescribed with vertical displacements estimated from the final folded form in Fig. 9(b) listed in Table 4. The predicted final configuration is shown in Fig. 10(a) and 10(b) in different views. ABAQUS takes 11 increments and 0.7 second of CPU time to complete the computation. Fig. 10(b) shows that the largest value of the maximum principal membrane strain is around 1.41%, justifying the small strain assumption. The animation video is given in Online Resource 7.
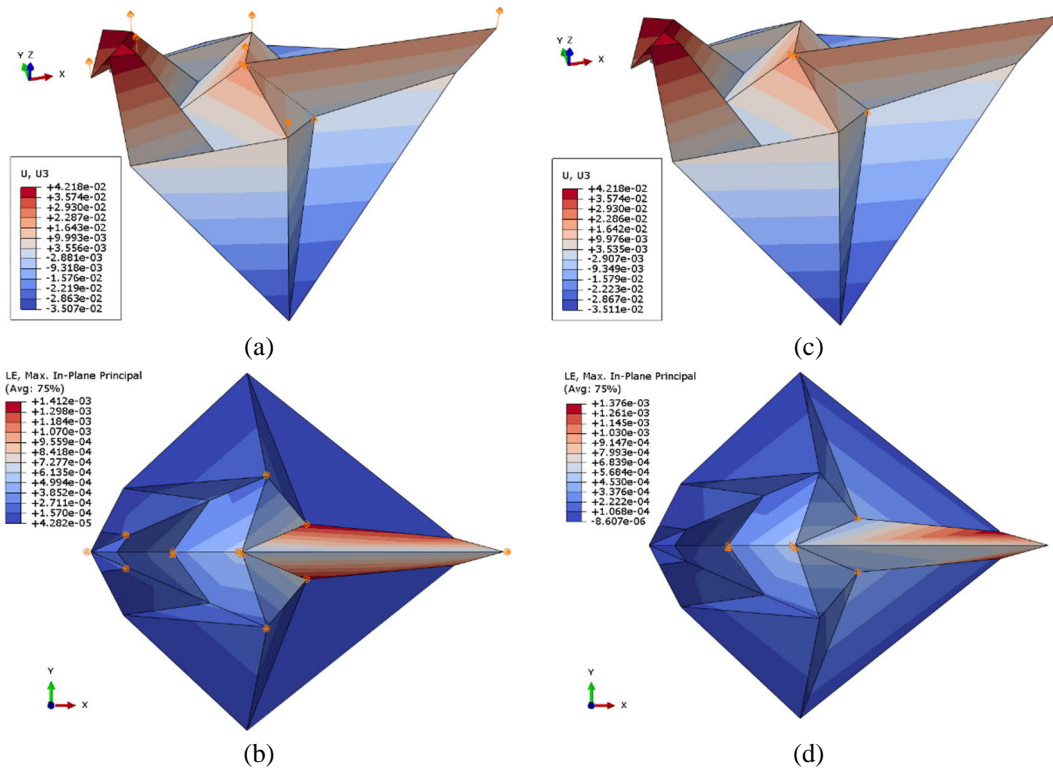

Fig. 10 Crane under displacement loading (a) and (b): (a) isometric view of the final configuration and the *Z*-displacement plot, (b) top view of the final configuration and the maximum principal membrane strain plot. (c) and (d) are the predictions under rest angle loading.

Table 4 Displacement loading conditions for the crane.

Nodes	A_5, A_6	A_{10}	A_1	A_9	A_7, A_8
Prescribed W	10.5×10^{-3}	22.0×10^{-3}	22.5×10^{-3}	26.3×10^{-3}	40.5×10^{-3}

In the rest angle loading case, the final rest angles for mountain and valley creases in Fig. 9(a) are set to be

$$\theta_{rest} = \begin{cases} \pi/2 & \text{for valley creases} \\ -\pi/2 & \text{for mountain creases} \end{cases}$$

ABAQUS takes 13 increments and 1.2 seconds of CPU time to complete the computation. The final configuration is shown in Fig. 10(c) and 10(d) which resembles that of the displacement loading in Fig. 10(a) and 10(d). The maximum principal membrane strain is plotted in Figure 10(d) and the largest value is 1.37%. The animation video is given in Online Resource 8. Since whether a crease is a valley or mountain type can be told readily, it is more straightforward to prescribe rest angles than the nodal displacements at the expense of higher computational cost.

To reduce the computational cost, it is straight forward to use symmetric condition in the displacement loading but slave image nodes would be needed in the rest angle loading. However, origami simulation often aims at seeing the whole origami. Hence, we choose to model the whole origami.

5.4. Compressing the Miura-ori and the derived Kirigami

This example considers the folding of a Miura-ori and its derived kirigami under displacement compression (Liu and Paulino 2017). Fig. 11(a) shows the flat Miura unit cell which is made up of four identical parallelograms with $a = b = 0.02$ and $\alpha = 60°$.

The Miura-ori consists of 5×5-unit cells. In the flat configuration, $\beta = 120°$, $L = L_{flat} = 0.1\sqrt{3} \approx 0.173$ and $W = W_{flat} = 0.2$. To avoid the buckling instability under the compressive loading, the initial configuration in Fig. 11(b) is taken to be nearly flat ($\beta = 118.27°$) but not perfectly flat. On the supporting conditions, node O is fixed; the nodes at $X = 0$ are on the same vertical plane and their X-displacements are fixed. The nodes at the other end of X (≈ 0.172) are on another vertical plane and their X-displacements are prescribed to be -0.16 under the compressive loading. For nodes on the X-Y-plane at the two ends, their Z-displacements are fixed.

The kirigami in Fig. 11(c) is obtained by cutting away 32 facets from the Miura-ori. Here, the paperboard is still adopted as the facet material. For the structures to behave like a mechanism with rigid panels connected by hinges, the ratio k/D should be small (Liu and Paulino 2017). To benchmark the predictions with the analytical solution based on the rigid facet assumption, the fold stiffness is reduced to $k = 10^{-4}$. With the setting, the kirigami experiences convergence problem. In this light, its initial time increment is set to be 0.01 whilst that of the Miura-ori remains to be 1.
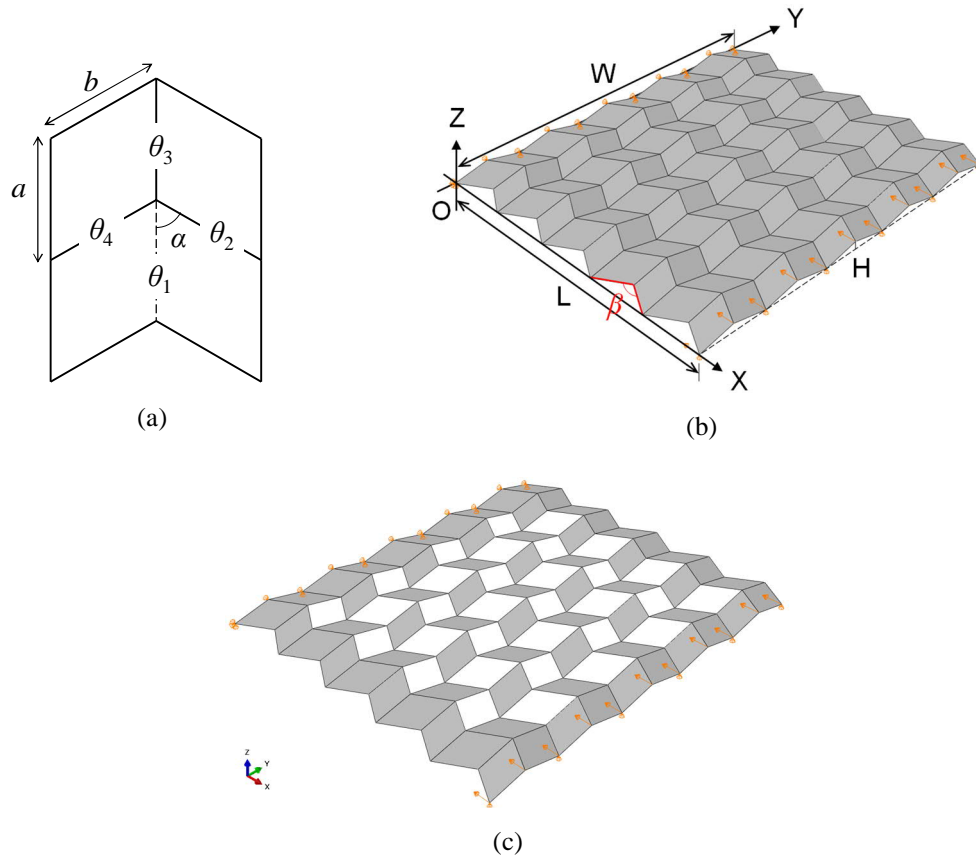
Fig. 11 (a) The flat Miura-ori unit cell: $a = b = 0.02$, $\alpha = 60°$; θ_is are fold angles at the creases. (b) The Miura-ori with 5×5 unit cells and $\beta = 118.27°$. (c) The kirigami obtained by cutting away 32 facets from the Miura-ori.

The width and height against the folding ratio are plotted in Fig. 12(a) for Miura-ori. The predictions agree well with the analytical solutions based on the rigid facet assumption (Wei et al. 2013). The dimensional changes of the kirigami are similar to those of the complete tessellation. The two partially folded configurations at $L/L_{flat} = 0.87$ and 0.55 are shown in Fig. 12(b) and (c). Fig. 13(a) and 13(b) show the histories of the crease energy and the reaction force (*X*-component) at the compressed end, respectively. They are essentially identical to the analytical solutions. Since the stiffness of the crease is much smaller than that of the facet, the deformation is confined to crease folding whilst the membrane and bending energies are negligible. Based on the rigid facet assumption, it is known that $\theta_3 = -\theta_1$ (minor folds) and $\theta_4 = \theta_2$ (major folds), see Figure 11(a) for the labels, during the folding process (Lang, Howell 2018). The Miura-ori has 90 minor and major folds whilst this number decreases to 26 for the kirigami. Thus, U_c for the Miura-ori : U_c for the kirigami = 90 : 26. The numerical predictions are in good agreement with this ratio, see Figure 13(a). The same ratio also holds for the magnitude of the reaction force which is shown in Figure 13(b). The animation videos for Miura-ori and the derived kirigami are given in Online Resources 9 and 10, respectively.
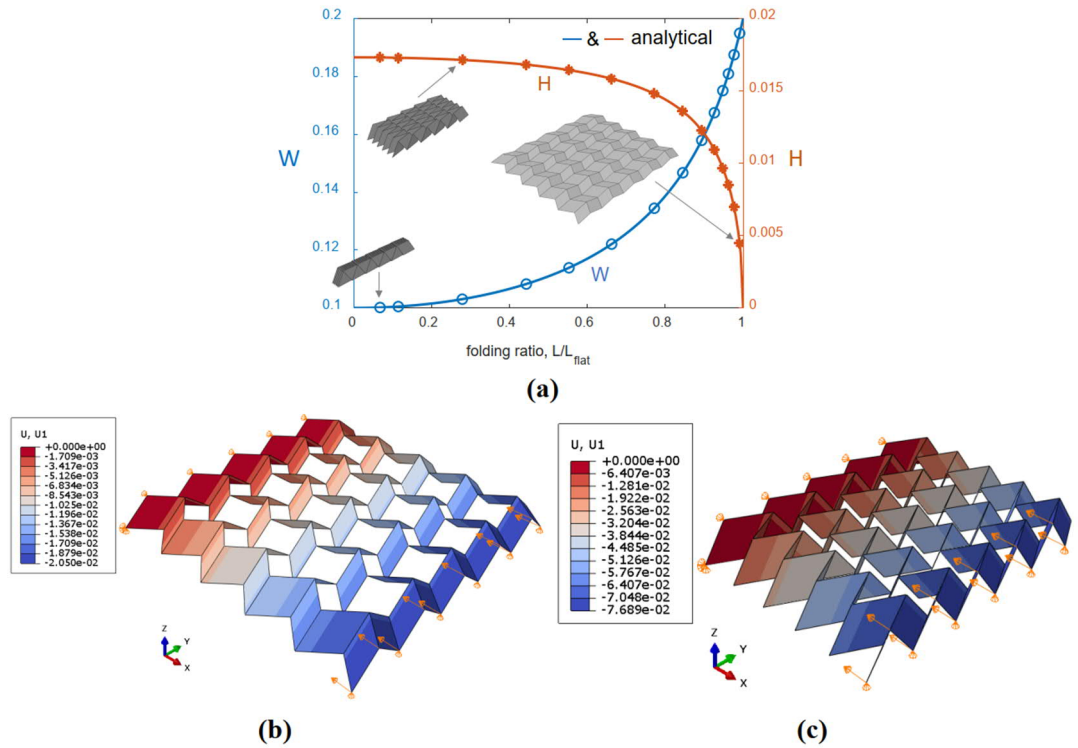
(a)

(b)   (c)

Fig. 12 (a) The width W and height H of the Miura-ori against the folding ratio (L/L_{flat}). "○" and "∗" are the numerical predictions whilst the solid lines are the analytical solutions. (b) and (c) are partially folded configurations of the Kirigami at $L/L_{flat} = 0.87$ and 0.55, respectively.
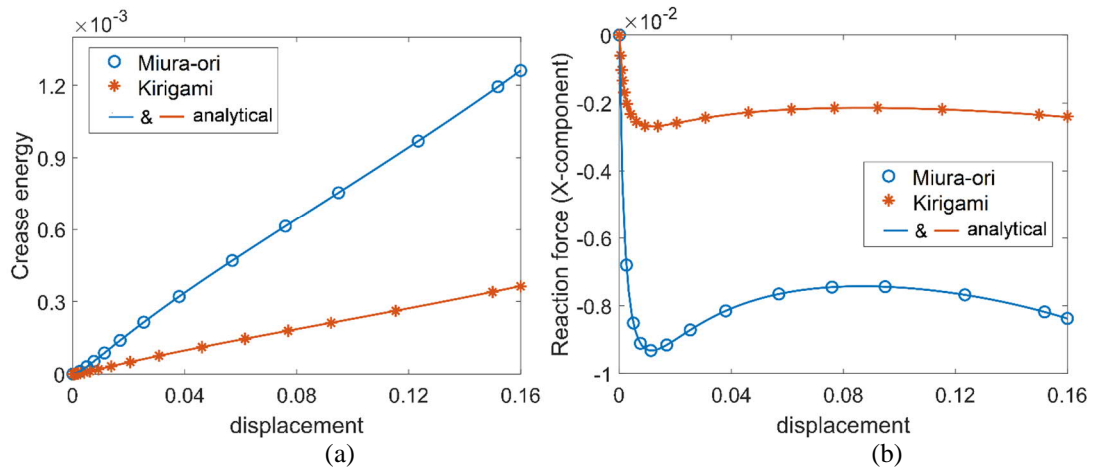

(a)   (b)

Fig. 13 (a) The crease energy and (b) the reaction force (X-component) at the compressed end for the Miura-ori and the Kirigami.

5.5. Pinching the Miura-ori and the derived Kirigami

This example considers the Miura-ori and its derived kirigami pinched at nodes A and B, see Fig. 14(a) and (b). Node B is fixed whilst node A is prescribed with $U = W = 0$ and $V = -0.03$. Node C is restrained from moving along the X-direction to avoid the rigid body rotation about the Y-axis. The

crease stiffness per unit length is $k = 1$ and β equals 90° in the initial configuration. The other settings are the same as the previous example except that the initial time step for the kirigami resumes to 1. Fig. 15(a) shows the final configuration for the Miura-ori which resembles a saddle and is in agreement with the experiment (Schenk, Guest 2011). To quantify the curved surface, a polynomial surface of degree 2 in both X and Y is constructed by least-square fit using the marked nodes in Fig. 14(a) and 14(b). The curvatures κ_x and κ_y at node C are evaluated (Liu, Paulino 2017). The histories of the curvatures and reaction force (Y-component) are plotted against the displacement $-V_A$ in Fig. 15(b). The results for the kirigami are shown in Fig. 15(c) and 15(d). For both structures, κ_x and κ_y vary almost linearly with the displacement. Due to the removed facets, the reaction force of the kirigami is much lower than that of the Miura-ori. Moreover, the final configuration of kirigami is shallower than that of the Miura-ori, see Fig. 15(a) and 15(c). This is also reflected by the magnitudes of the curvature in Fig. 15(b) and 15(d). The animation videos for Miura-ori in the two different views are given in Online Resources 11 and 12 whilst those for the derived kirigami are given in Online Resources 13 and 14.

5.6. Kresling tube under compression

The Kresling pattern is a well-known origami pattern for deployable cylindrical tubes (Kresling 2008; Guest and Pellegrino 1994). The tube considered here consists of three layers along Z-axis and each layer is made up of 16 identical triangular facets as shown in Fig. 16(a). There is no quadrilateral facet. The initial configuration is folded. It is specified by the height of the layer $H = 0.05$ and the radius of circumscribed circle $R = H$, see Fig. 16(b). The Z-displacement W of the bottommost nodes A_1 to A_8 at $Z = 0$ are set to zero. To avoid rigid body movements, U at A_3 and A_7 are set to zero whilst V at A_1 is set to zero. The topmost nodes at $Z = 3H$ are prescribed with $W = -3H$ for compressing the tube. Fig. 17(a), 17(b) and 17(c) plot the vertical reaction force, energies and maximum principle stress against the normalized vertical displacement of the topmost nodes, respectively. Since this problem converges very rapidly, the initial and maximum time increments are respectively set to be 0.01 and 0.02 to enable a fine tracing of the load history. The reaction force first decreases from 0 to the minimum -1300 at $W/H \approx -0.27$. The force then increases and becomes positive at $W/H \approx -1$ and thereafter. The reaction force equals to zero at $W/H = 0$, ≈ -1 and $= -3$. For $0 > W/H > -1$, a download force is required to compress the tube. For $-1 > W/H > -3$, the tube would continue to retract by itself. From the reaction force and the total energy plots, the equilibriums are stable at $W/H = 0$ and -3 whilst the equilibrium is unstable at $W/H \approx -1$. Hence, the tube is bi-stable (Jianguo et al. 2015; Liu, Paulino 2017). The animation video is given in Online Resource 15.
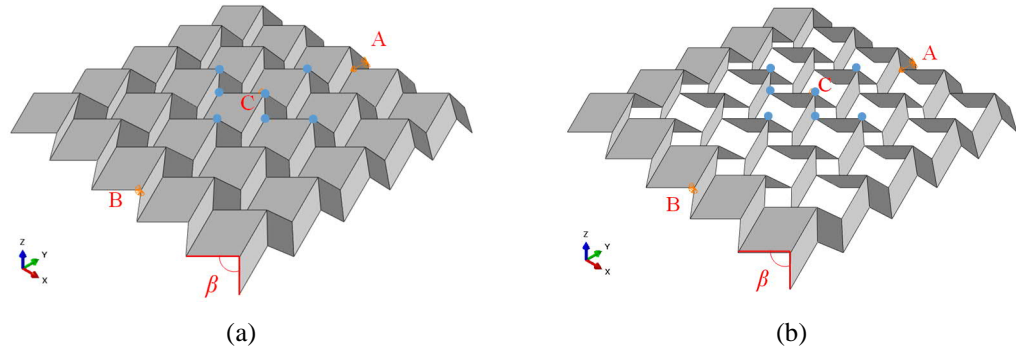
(a)   (b)

Fig. 14 The initial configurations of (a) the Miura-ori and (b) the kirigami in which $\beta = 90°$.

(a)   (c)

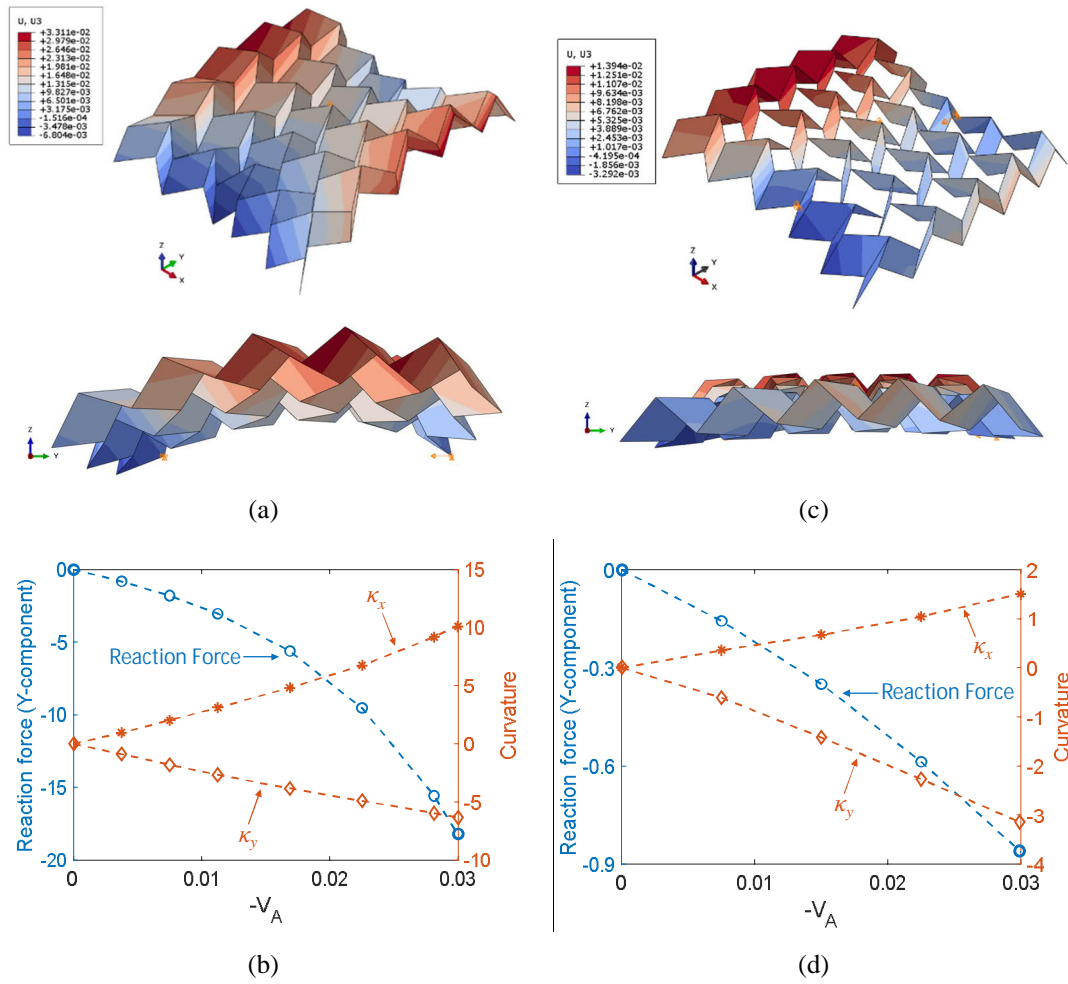(b)   (d)

Fig. 15 The Miura-ori under pinching: (a) the isometric and side views of final configuration with the contour showing the Z-displacement, (b) the history of the reaction force (Y-component) at node A and the curvatures κ_x and κ_y. (c) and (d) are the predictions for the kirigami.
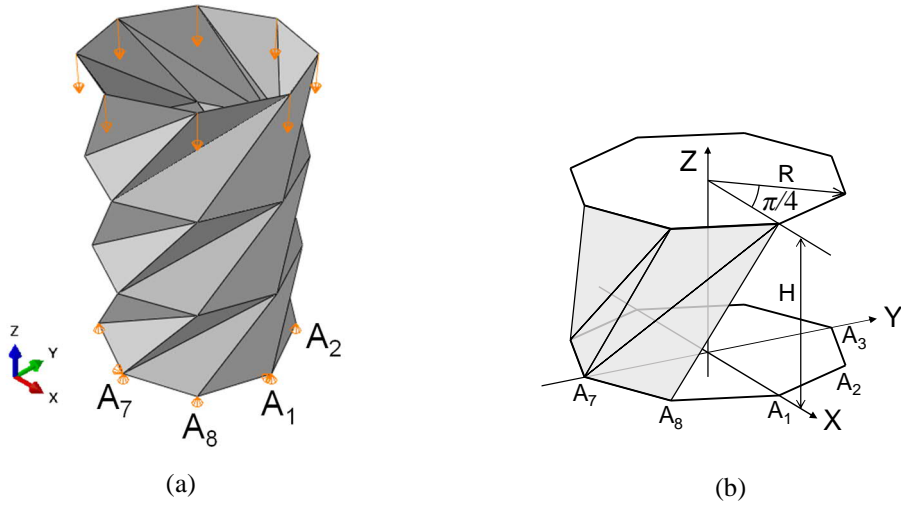
23

Fig. 16 (a) The initial Kresling tube. The bottommost and topmost nodes are constrained with the Z-displacement 0 and -3*H*, respectively. (b) The bottommost layer of the tube. $H = R = 0.05$.
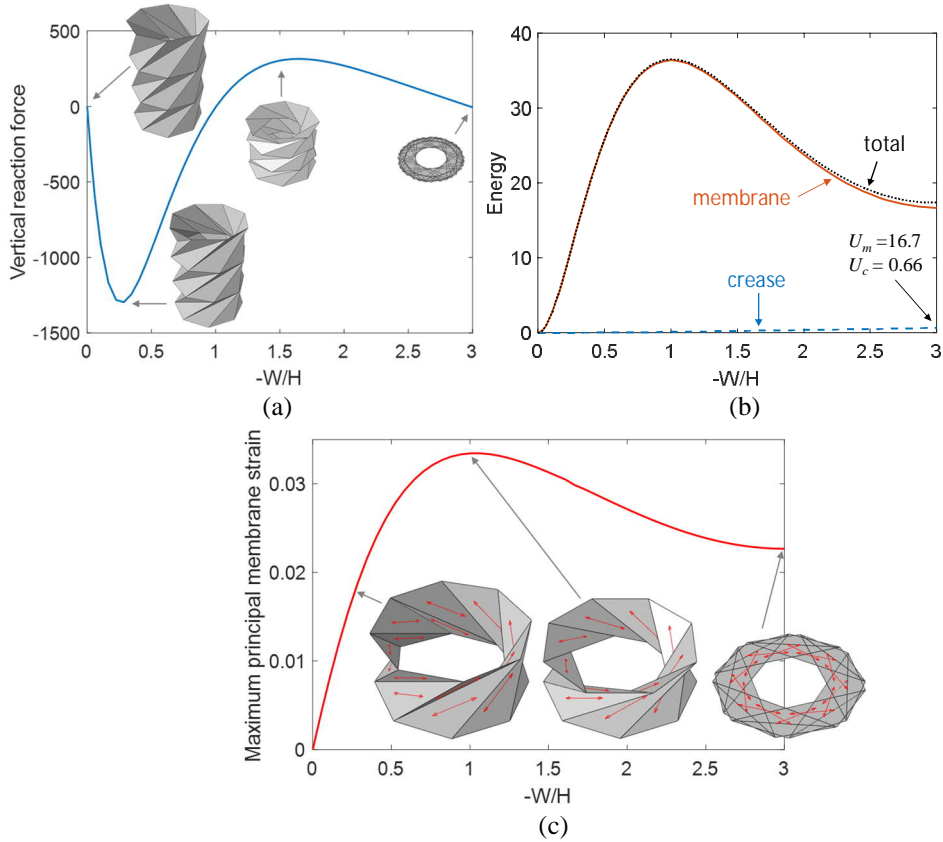

Fig. 17 Results for the Kresling tube plotted against the deflection: (a) the vertical reaction force; (b) the crease and total energies; (c) the maximum principal membrane strain

5.7. Small Strain Small Curvature Assumption

The small strain small curvature assumption is adopted in the derivation of the Q4 bending and the 4-node crease elements. To justify the assumption, the maximum first principal membrane strain ε_1 and

24

the maximum $\Delta w/\sqrt{j_0}$ among all the elements at the end of last all successfully completed time increments are traced and listed in Table 5. It can be seen that the maximum ε_1 is only 3.34% which is acceptable for small strain assumption. The small curvature assumption is more complicated. One should look at the ratio of the element size and the radius of curvature but not the curvature alone. In Appendix A, the square element geometry is assumed for simplicity and the maximum $\Delta w/\sqrt{j_0} = 0.424$ is employed to compare the curvatures computed by the small curvature assumption in (5) and obtained by fitting the deformed surface with circular arcs. The curvatures obtained by the two approaches differ only by 0.33%. Though the analysis involves approximations, the difference in the two curvatures is sufficiently small for adopting the small curvature assumption.

Table 5 Maximum ε_1 and maximum $\Delta w/\sqrt{j_0}$ among all the elements.

	Maximum ε_1	Maximum $\Delta w/\sqrt{j_0}$
Elastic Hinge (see Section 5.1)	0.000%	0.000
Pop-up Kirigami using rest angle loading (see Section 5.2)	0.000%	0.000
Pop-up Kirigami using displacement loading (see Section 5.2)	0.046%	0.030
Crane using rest angle loading (see Section 5.3)	0.058%	0.081
Crane using displacement loading (see Section 5.3)	1.02%	0.132
Compressing Miura-ori (see Section 5.4)	0.000%	0.001
Compressing the derived Kirigami (see Section 5.4)	0.001%	0.003
Pinching Miura-ori (see Section 5.5)	1.71%	0.424
Pinching the derived Kirigami (see Section 5.5)	0.22%	0.173
Kresling tube under compression (see Section 5.6)	3.34%	n.a.*

* Q4 elements are not employed.

6. CLOSURE

A Q4 bending element and a 4-node crease element are developed in this paper for origami simulation. To account for the bending energy in the Q4 bending element, a corotational consideration is taken. Based on large displacement/rotation but small strain/curvature behaviour of the facet, the energy turns out to be a quadratic function of the nodal displacement. Thus, the relevant tangential stiffness matrix is constant and requires no update in the iterative solution process. On the other hand, the fold angle in the crease element is quantified by using the dot product of two vectors connecting the crease and the nodes defining the two adjacent facets. The complexity in the derivatives of the fold angle with respect to the nodal displacement is considerably reduced by invoking the small strain/curvature behaviour of the facet. The crease element is equally applicable to elastic hinge modelling. The proposed elements are implemented in ABAQUS thru two user-defined element subroutines, see Appendix B, and co-used with of 3D membrane elements in ABAQUS. Indeed, it is straight forward to program a comprehensive Q4 element which takes both the membrane and bending deformations into account. Since ABAQUS

does not show user-defined elements in its post-processor, the 3D membrane elements of ABAQUS are purposely employed such that the predicted geometry can be displayed by the software. Validation examples including elastic hinge, origami and kirigami are presented whilst the pertinent videos are provided in the Online Resources 1 to 15. The ABAQUS input (.INP) files and FORTRAN source (.FOR) files required to run the example on the crane in Section 5.3 are provided in Online Resources 16 and 17 for the displacement loading and 18 and 19 for the rest-angle loading. Interested readers may contact the authors for files on other examples. Though not explored in this paper, instability of the origami can also be studied using the built-in Riks solution method in ABAQUS.

REFERENCES

Bekker, H.: Molecular dynamics simulation methods revised. Rijksuniversiteit Groningen, (1996)

Bischoff, M., Ramm, E.: Shear deformable shell elements for large strains and rotations. International Journal for Numerical Methods in Engineering **40**(23), 4427-4449 (1998)

Bischoff, M., Ramm, E., Irslinger, J.: Models and finite elements for thin-walled structures. Encyclopedia of Computational Mechanics Second Edition, 1-86 (2018)

Crisfield, M.A.: Non-Linear Finite Element Analysis of Solids and Structures Volume 2: Advanced Topics. Chichester: Wiley (2000)

Filipov, E.T., Liu, K., Tachi, T., Schenk, M., Paulino, G.H.: Bar and hinge models for scalable analysis of origami. International Journal of Solids and Structures **124**, 26-45 (2017)

Flores, F.G., Oñate, E.: Wrinkling and folding analysis of elastic membranes using an enhanced rotation-free thin shell triangular element. Finite Elements in Analysis and Design **47**(9), 982-990 (2011)

Ghassaei, A., Demaine, E.D., Gershenfeld, N.: Fast, interactive origami simulation using GPU computation. Origami **7**, 1151-1166 (2018)

Gillman, A., Fuchi, K., Buskohl, P.R.: Truss-based nonlinear mechanical analysis for origami structures exhibiting bifurcation and limit point instabilities. International Journal of Solids and Structures **147**, 80-93 (2018)

Grey, S.W., Scarpa, F., Schenk, M.: Strain Reversal in Actuated Origami Structures. Physical Review Letters **123**(2), 025501 (2019)

Guest, S.D., Pellegrino, S.: The folding of triangulated cylinders, part II: the folding process. (1994)

Guo, Y.Q., Gati, W., Naceur, H., Batoz, J.L.: An efficient DKT rotation free shell element for springback simulation in sheet metal forming. Computers & structures **80**(27-30), 2299-2312 (2002)

Hauptmann, R., Schweizerhof, K.: A systematic development of "solid-shell" element formulations for linear and non-linear analyses employing only displacement degrees of freedom. International Journal for Numerical Methods in Engineering **42**(1), 49-69 (1998)

Cai J.G., Deng X.W., Zhou Y., Feng J., Tu Y.M.: Bistable behavior of the cylindrical origami structure with Kresling pattern. Journal of Mechanical Design **137**(6) (2015)

Kim, C.H., Sze, K.Y., Kim, Y.H.: Curved quadratic triangular degenerated- and solid- shell elements for geometric nonlinear analysis. International Journal for Numerical Methods in Engineering **57**(14), 2077-2097 (2003)

Kim, Y.H., Lee, S.W.: A solid element formulation for large deflection analysis of composite shell structures. In: Computational Structural Mechanics & Fluid Dynamics. pp. 269-274. Elsevier, (1988)

Kresling, B.: Natural twist buckling in shells: from the hawkmoth's bellows to the deployable Kresling-pattern and cylindrical Miura-ori. In: Proceedings of the 6th International Conference on Computation of Shell and Spatial Structures, John F. Abel and J. Robert Cooke, eds., Ithaca 2008, pp. 12-32

Kulikov, G.M., Plotnikova, S.V.: Finite rotation geometrically exact four-node solid-shell element with seven displacement degrees of freedom. Computer Modeling in Engineering & Sciences **28**(1), 15-38 (2008)

Lang, R.J., Howell, L.: Rigidly foldable quadrilateral meshes from angle arrays. Journal of Mechanisms and Robotics **10**(2) (2018)

Lechenault, F., Thiria, B., Adda-Bedia, M.: Mechanical response of a creased sheet. Physical Review Letters **112**(24), 244301 (2014)

Lee, T.-U., Yang, X.C., Ma, J.Y., Chen, Y., Gattas, J.M.: Elastic buckling shape control of thin-walled cylinder using pre-embedded curved-crease origami patterns. International Journal of Mechanical Sciences **151**, 322-330 (2019)

Liu, K., Paulino, G.H.: Nonlinear mechanics of non-rigid origami: an efficient computational approach. Proceedings of the Royal Society A: Mathematical, Physical and Engineering Sciences **473**(2206), 20170348 (2017)

Liu, K., Tachi, T., Paulino, G.H.: Invariant and smooth limit of discrete geometry folded from bistable origami leading to multistable metasurfaces. Nature communications **10**(1), 1-10 (2019)

Ma, J.Y., Song, J.C., Chen, Y.: An origami-inspired structure with graded stiffness. International Journal of Mechanical Sciences **136**, 134-142 (2018)

Ma, J.Y., You, Z.: Energy absorption of thin-walled beams with a pre-folded origami pattern. Thin-Walled Structures **73**, 198-206 (2013)

Miura, K.: Method of packaging and deployment of large membranes in space. Title The Institute of Space and Astronautical Science Report **618**, 1 (1985)

Nelson, T.G., Zimmerman, T.K., Lang, R.J., Magleby, S.P., Howell, L.L.: Developable mechanisms on developable surfaces. (2019)

Park H.C., Cho C., Lee S.W.: An efficient assumed strain element model with 6 dof per node for geometrically nonlinear shells. International Journal for Numerical Methods in Engineering **38**(24), 4101–4122 (1995).

Pratapa, P.P., Liu, K., Paulino, G.H.: Geometric mechanics of origami patterns exhibiting Poisson's ratio switch by breaking mountain and valley assignment. Physical Review Letters **122**(15), 155501 (2019)

Schenk, M., Guest, S.D.: Origami folding: A structural engineering approach. Origami **5**, 291-304 (2011)

Schenk, M., Guest, S.D.: Geometry of Miura-folded metamaterials. Proceedings of the National Academy of Sciences **110**(9), 3276-3281 (2013)

Schulgasser, K.: The in-plane Poisson ratio of paper. Fibre Science and Technology **19**(4), 297-309 (1983)

Song, J., Chen, Y., Lu, G.X.: Axial crushing of thin-walled structures with origami patterns. Thin-Walled Structures **54**, 65-71 (2012)

Sze, K.Y.: Three-dimensional continuum finite element models for plate/shell analysis. Progress in Structural Engineering and Materials **4**(4), 400-407 (2002)

Sze, K.Y., Chan, W.K., Pian, T.H.H.: An eight-node hybrid-stress solid-shell element for geometric non-linear analysis of elastic shells. International Journal for Numerical Methods in Engineering **55**(7), 853-878 (2002)

Sze, K.Y., Liu, X.H., Lo, S.H.: Popular benchmark problems for geometric nonlinear analysis of shells. Finite elements in Analysis and Design **40**(11), 1551-1569 (2004)

Sze, K.Y., Liu, X.H.: A corotational interpolatory model for fabric drape simulation. International Journal for Numerical Methods in Engineering **77**(6), 799-823 (2009)

Tachi, T.: Simulation of rigid origami. Origami **4**(8), 175-187 (2009)

Wei, Z.Y., Guo, Z.V., Dudte, L., Liang, H.Y., Mahadevan, L.: Geometric mechanics of periodic pleated origami. Physical Review Letters **110**(21), 215501 (2013)

Zhai, Z.R., Wang, Y., Jiang, H.Q.: Origami-inspired, on-demand deployable and collapsible mechanical metamaterials with tunable stiffness. Proceedings of the National Academy of Sciences **115**(9), 2032-2037 (2018)

Zhang, X., Chen, Y.: Mobile assemblies of Bennett linkages from four-crease origami patterns. Proceedings of the Royal Society A: Mathematical, Physical and Engineering Sciences **474**(2210), 20170621 (2018)

Zhou, Y.X., Sze, K.Y.: A geometric nonlinear rotation-free triangle and its application to drape simulation. Journal for Numerical Methods in Engineering **89**(4), 509-536 (2012)

Zirbel, S.A., Lang, R.J., Thomson, M.W., Sigel, D.A., Walkemeyer, P.E., Trease, B.P., Magleby, S.P., Howell, L.L.: Accommodating thickness in origami-based deployable arrays. Journal of Mechanical Design **135**(11) (2013)

Appendix A Curvature

To assess the accuracy of the equations on the curvature components in terms of Δw in (7), the square element shown in Figure A.1(a) is considered. For the element, the geometric parameters defined under (2) and (3) are

$$a_0 = b_0 = a_2 = b_2 = 0, \ a_1 = -b_1 = a_3 = b_3 = L/2, \ j_0 = L^2/2 \ , \ j_1 = j_2 = 0. \tag{A1}$$
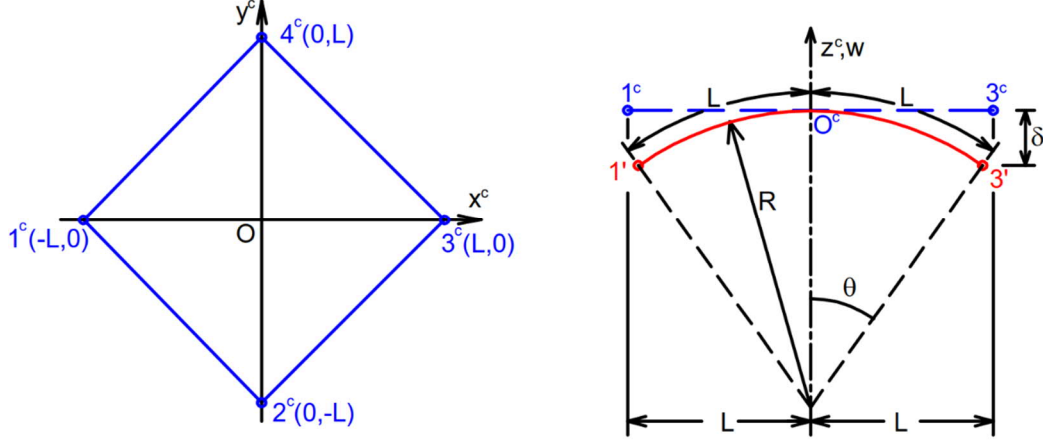

Figure A.1 (a) A square element and its corotated local coordinates (x,y). (b) The corotated configuration 1^c-O^c-3^c and the final deformed configuration $1'$-O^c-$3'$ of the element on the x^c-z^c plane.

With the local displacement from the co-rotational to the final deformed configuration taken to be $w_1 = w_3 = -\delta$ and $w_2 = w_4 = \delta$, (5) and (6) becomes

$$\Delta w = -2\delta, \ \frac{\partial^2 w}{\partial^2 x^c} = -\frac{2\delta}{L^2} \ , \ \frac{\partial^2 w}{\partial^2 y^c} = \frac{2\delta}{L^2} \ , \ \frac{\partial^2 w}{\partial x^c \partial y^c} = 0 \tag{A2}$$

For the curvature along 1^c and 3^c, the local transverse plane through 1^c and 3^c in Figure A.1 is considered. The final deformed location of the two nodes are $1'$ and $3'$. The element centre in the corotational configuration is O^c and its local displacement is zero. To obtain the exact curvature, the arc through $1'$, 0^c and $3'$ is constructed whilst the arc length can be approximated as $2L$ under the small strain assumption. With the angle subtended by the arc be 2θ, the geometry gives

$$R\theta = L , \ \cos\theta = \frac{R-\delta}{R} \tag{A3}$$

from which

$$\frac{\delta}{L} = \frac{R}{L}(1 - \cos\frac{L}{R}) \tag{A4}$$

It can be taken as the reference solution. On the other hand, the second expression in (A2) is an approximation to $-1/R$ based on the small curvature assumption. It can be rewritten as

$$\frac{\delta}{L} = \frac{1}{2}\frac{L}{R} \tag{A5}$$

The last two relations between δ/L and the normalized curvature are plotted in Figure A.2.
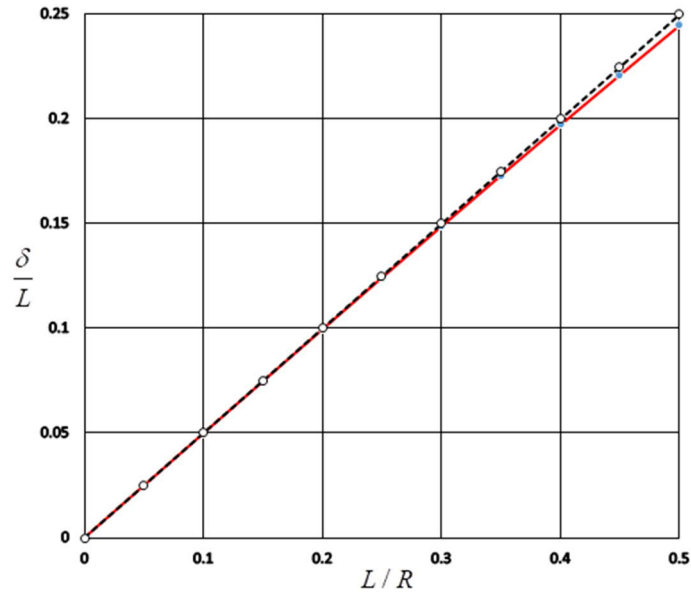
Figure A.2 The relations between δ/L and the normalized curvature L/R.
—— gives the relation in (A4), - - - gives the relation in (A5).

Among the numerical predictions in Section 5.7, the highest value of $|\Delta w|/\sqrt{jo}$ is 0.424. When the above square element geometry is assumed as an approximation, the value leads to $\delta/L = 0.150$ for which the relations in (A4) and (A5) give $L/R = 0.302$ and 0.300, respectively. The difference is 0.33%. Even if one add another 50% to δ/L which becomes 0.225, the relations in (A4) and (A5) give $L/R = 0.457$ and 0.450, respectively. The difference is 1.5% which is still small. The identical differences can be obtained for the curvature along the y^c-direction.

Appendix B Abaqus UEL Subroutine

```fortran
subroutine uel(rhs,amatrx,svars,energy,ndofel,nrhs,nsvars,
1      props,nprops,coords,mcrd,nnode,u,du,v,a,jtype,time,dtime,
2      kstep,kinc,jelem,params,ndload,jdltyp,adlmag,predef,
3      npredf,lflags,mlvarx,ddlmag,mdload,pnewdt,jprops,njprop,
4      period)
include 'aba_param.inc'
dimension rhs(mlvarx,*),amatrx(ndofel,ndofel),
1      svars(*),energy(7),props(*),coords(mcrd,nnode),
2      u(ndofel),du(mlvarx,*),v(ndofel),a(ndofel),time(2),
3      params(*),jdltyp(mdload,*),adlmag(mdload,*),
4      ddlmag(mdload,*),predef(2,npredf,nnode),lflags(4),
5      jprops(*)
! (jtype = 1002) Q4 bending element
! (jtype = 1004) 4-node crease element
if (jtype==1002) then
     call quad_bending(time,kstep,kinc,jelem,MLVARX,NDOFEL,coords,
&      U,props,energy,svars,RHS,AMATRX)
elseif (jtype==1004) then
     call crease_hinge(time,kstep,kinc,jelem,jtype,
&      MLVARX,NDOFEL,coords,U,props,energy,svars,RHS,AMATRX)
endif
return
end subroutine


! 1002 for Q4 bending element
subroutine quad_bending(time,kstep,kinc,jelem,MLVARX,NDOFEL,coords,
&      U,props,energy,svars,RHS,AMATRX)
include 'aba_param.inc'
real*8 svars(*),RHS(MLVARX,*)
real*8 coords(3,4),U(NDOFEL),props(*),energy(7),AMATRX(NDOFEL,NDOFEL)
real*8 Eb(3,3),Vab(3),Vac(3),Vn1(3),Vad(3)
real*8 dl(3),bl(3),VI(3),LV(4),LF(4),Vpq(3)
real*8 Va(3)
real*8 a1,b1,a3,b3,j0,al(2),cl(2)
real*8 xi,lac,lbd,lpq,c0,x0,kL,k1,k0,Db,kac,eac
integer i,j,ki,kj
real*8 norm

! Find the point of intersection,  VI
Vab=coords(:,2)-coords(:,1)
Vac=coords(:,3)-coords(:,1)
Vad=coords(:,4)-coords(:,1)
call cross_product(Vab,Vac,Vn1)
Eb(:,3)=Vn1/norm(Vn1,3)
Eb(:,1)=Vac/norm(Vac,3)
call cross_product(Eb(:,3),Eb(:,1),Eb(:,2))

bl=matmul(Vab,Eb)  ! vertex b in the local coordinate
dl=matmul(Vad,Eb)  ! vertex d in the local coordinate
xi=-bl(2)/( dl(2)-bl(2) )*( dl(1)-bl(1) )+bl(1)
VI=coords(:,1)+xi*Eb(:,1)
do i=1,4
     Va=VI-coords(:,i)
     LV(i)=norm(Va,3)
enddo
```

```fortran
      lac=LV(1)+LV(3)
      lbd=LV(2)+LV(4)
      LF=(/ -LV(3)/lac, LV(4)/lbd, -LV(1)/lac, LV(2)/lbd /)

      ! 1002 for Q4 bending
      al=(/0.d0,0.d0/)
      cl=(/lac,0.d0/)
      a1=( -al(1)+bl(1)+cl(1)-dl(1) )/4.d0
      b1=( -al(2)+bl(2)+cl(2)-dl(2) )/4.d0
      a3=( -al(1)-bl(1)+cl(1)+dl(1) )/4.d0
      b3=( -al(2)-bl(2)+cl(2)+dl(2) )/4.d0
      j0=a1*b3-a3*b1
      c0=4.d0*(b1*b3+a1*a3)**2/(j0**3) + 2.d0*(1.d0-props(2))/j0
      k0=props(1)
      kL=k0*c0
      Vpq=0.d0
      do j=1,4
          ki=(j-1)*3+1
          kj=j*3
          Vpq=Vpq+LF(j)*U(ki:kj)
      enddo

      energy(2)=kL/2.d0*dot_product(Vpq,Vpq)
      Ipq=dot_product(Vpq,Vpq)
      Ipq=sqrt(Ipq)
      kac=Ipq/j0
      eac=Ipq/sqrt(j0)
      svars(1:4)=LV
      svars(5)=c0

      ! RHS and AMATRX
      do j=1,4
          do i=1,3
              ki=(j-1)*3+i
              RHS(ki,1)=-kL*Vpq(i)*LF(j)
          enddo
      enddo
      do j=1,4
          do i=1,4
              ki=(i-1)*3
              kj=(j-1)*3
              x0=kL*LF(i)*LF(j)
              AMATRX(ki+1,kj+1)=x0
              AMATRX(ki+2,kj+2)=x0
              AMATRX(ki+3,kj+3)=x0
          enddo
      enddo
      return
      end subroutine


      ! U1004 for the 4-node crease element
      subroutine crease_hinge(time,kstep,kinc,jelem,jtype,
     &  MLVARX,NDOFEL,coords,U,props,energy,svars,RHS,AMATRX)
      include 'aba_param.inc'
      parameter pi=3.1415926535897932384626433832795d0
      real*8 svars(*),RHS(MLVARX,*),time(*)
      real*8 coords(3,4),U(NDOFEL),props(*),energy(7),AMATRX(NDOFEL,NDOFEL)
      real*8 Un(3,4),ndx(3,4)
```

```fortran
      real*8 mom,kL,he0
      real*8 lab,he
      real*8 dD(3),dC(3),dA(3),dB(3),Jhe(12)
      real*8 dCC(3,3),dCD(3,3),dCA(3,3),dCB(3,3)
      real*8 dDD(3,3),dDA(3,3),dDB(3,3)
      real*8 dAA(3,3),dAB(3,3),dBB(3,3)
      integer i,j,ki,kj,num(4)
      real*8 norm
      real*8 tfav(13), fav(13) ! modify this

      ! prescribe the rest angles, he0
      ! call fold_angle(coords,he0) ! used for displacement loading
      fav =0.d0
      tfav=0.d0
      num=(/6,8,4,10/)
      tfav(num)= pi/2.d0
      tfav(  7)=-pi/2.d0
      he0=(1.d0-time(1))*fav(jelem-1000) + time(1)*tfav(jelem-1000)

      ! calculate the derivative and Hessian matrix
      call JHess_PQ(U,coords,lab,he,dC,dD,dA,dB,
     &   dCC,dCD,dCA,dCB,dDD,dDA,dDB,dAA,dAB,dBB)

      ! moment and energy
      kL=props(1)*lab
      mom=kL*(he-he0)
      energy(2)=kL/2.d0*(he-he0)**2

      ! RHS
      Jhe=(/dA,dC,dB,dD/)
      RHS(:,1)=-mom*Jhe

      ! AMATRX, Note that dAC=Transpose(dCA)=dCA
      AMATRX(1:3,1:3)=dAA
      AMATRX(1:3,4:6)=dCA
      AMATRX(1:3,7:9)=dAB
      AMATRX(1:3,10:12)=dDA

      AMATRX(4:6,1:3)=   dCA
      AMATRX(4:6,4:6)=   dCC
      AMATRX(4:6,7:9)=   dCB
      AMATRX(4:6,10:12)=dCD

      AMATRX(7:9,1:3)=dAB
      AMATRX(7:9,4:6)=dCB
      AMATRX(7:9,7:9)=dBB
      AMATRX(7:9,10:12)=dDB

      AMATRX(10:12,1:3  )=dDA
      AMATRX(10:12,4:6  )=dCD
      AMATRX(10:12,7:9  )=dDB
      AMATRX(10:12,10:12)=dDD

      AMATRX=mom*AMATRX
      do j=1,12
         do i=1,12
             AMATRX(i,j)=AMATRX(i,j)+kL*Jhe(i)*Jhe(j)
         enddo
      enddo
```

```fortran
        return
      end subroutine

! Calculate the derivative and Hessian matrix
      subroutine JHess_PQ(U,coords,lab,he,dC,dD,dA,dB,
&        dCC,dCD,dCA,dCB,dDD,dDA,dDB,dAA,dAB,dBB)
      include 'aba_param.inc'
      parameter pi=3.1415926535897932384626433832795d0
      real*8 U(12),coords(3,4),he,lab
      real*8 dD(3),dC(3),dA(3),dB(3)
      real*8 dCC(3,3),dCD(3,3),dCA(3,3),dCB(3,3)
      real*8 dDD(3,3),dDA(3,3),dDB(3,3)
      real*8 dAA(3,3),dAB(3,3),dBB(3,3)
      real*8 vab(3),eab(3),XP(3),XQ(3),eba(3)
      real*8 vpc(3),vqd(3),vtemp(3)
      real*8 sp(2),sq(2),lpc,lqd,pq
      real*8 ct,st,Un(3,4),ndx(3,4)
      real*8 iab(3),iac(3),iad(3),ilab
      real*8 cpn(3),cnq(3)
      real*8 norm

! sp and sq calculated from the inital configuration
      iab=coords(:,3)-coords(:,1)
      iac=coords(:,2)-coords(:,1)
      iad=coords(:,4)-coords(:,1)
      ilab=norm(iab,3)
      sp(2)=dot_product(iac,iab)/ilab/ilab
      sq(2)=dot_product(iad,iab)/ilab/ilab
      sp(1)=1.d0-sp(2)
      sq(1)=1.d0-sq(2)

! the current configuration
      Un=reshape(U,(/3,4/))
      ndx=coords+Un

! vectors
      vab=ndx(:,3)-ndx(:,1)
      lab=norm(vab,3)
      eab=vab/lab
      eba=-eab
      XP=sp(1)*ndx(:,1)+sp(2)*ndx(:,3)
      XQ=sq(1)*ndx(:,1)+sq(2)*ndx(:,3)
      vpc=ndx(:,2)-XP
      vqd=ndx(:,4)-XQ
      lpc=norm(vpc,3)
      lqd=norm(vqd,3)
      pq=lpc*lqd

! fold angle
      ct=-dot_product(vpc,vqd)/pq
      call cross_product(vpc,vqd,vtemp)
      vtemp=-vtemp/pq
      st=dot_product(vtemp,eab)
      he=atan2(st,ct)

! first order derivatives
      call cross_product(vpc,eba,cpn)
      call cross_product(eba,vqd,cnq)
      dC=-cpn/lpc/lpc
```

34

```fortran
      dD=-cnq/lqd/lqd
      dA=-sp(1)*dC-sq(1)*dD
      dB=-sp(2)*dC-sq(2)*dD

      ! second order derivatives
      do j=1,3
          do i=1,3
              dCC(i,j)=cpn(i)*vpc(j)+cpn(j)*vpc(i)
              dDD(i,j)=cnq(i)*vqd(j)+cnq(j)*vqd(i)
          enddo
      enddo
      dCC=dCC/(lpc**4)
      dDD=dDD/(lqd**4)
      dCD=0.d0
      dCA=-sp(1)*dCC
      dCB=-sp(2)*dCC
      dDA=-sq(1)*dDD
      dDB=-sq(2)*dDD
      dAA=sp(1)*sp(1)*dCC + sq(1)*sq(1)*dDD
      dAB=sp(1)*sp(2)*dCC + sq(1)*sq(2)*dDD
      dBB=sp(2)*sp(2)*dCC + sq(2)*sq(2)*dDD
      return
end subroutine

! Calculate the fold angle
subroutine fold_angle(ndx,he)
 include 'aba_param.inc'
 parameter pi=3.14159265358979323846264338327950d0
 real*8 ndx(3,4),he
 real*8 vab(3),vac(3),vad(3),eab(3),eba(3)
 real*8 sp(2),sq(2),xp(3),xq(3),vpc(3)
 real*8 vqd(3),lab,lpc,lqd,pq,ct,st,vtemp(3)
 real*8 norm

 ! vectors
 vab=ndx(:,3)-ndx(:,1)
 vac=ndx(:,2)-ndx(:,1)
 vad=ndx(:,4)-ndx(:,1)

 lab=norm(vab,3)
 eab=vab/lab
 eba=-eab

 sp(2)=dot_product(vac,eab)/lab
 sq(2)=dot_product(vad,eab)/lab
 sp(1)=1.d0-sp(2)
 sq(1)=1.d0-sq(2)
 XP=sp(1)*ndx(:,1)+sp(2)*ndx(:,3)
 XQ=sq(1)*ndx(:,1)+sq(2)*ndx(:,3)
 vpc=ndx(:,2)-XP
 vqd=ndx(:,4)-XQ
 lpc=norm(vpc,3)
 lqd=norm(vqd,3)
 pq=lpc*lqd

 ! fold angle, atan2
 ct=-dot_product(vpc,vqd)/pq
 call cross_product(vpc,vqd,vtemp)
 vtemp=-vtemp/pq
```

```fortran
  st=dot_product(vtemp,eab)

 he=atan2(st,ct)
 return
end subroutine

! Calculate the L2 norm of a vector with n entries
real*8 function norm(a,n)
 implicit none
 real*8 a(n)
 integer n
 norm=dot_product(a,a);
 norm = sqrt(norm);
end function

! c = Cross product(a,b)
subroutine cross_product(a,b,c)
 implicit none
 real*8 a(3),b(3)
 real*8 c(3)
 c(1) = a(2)*b(3) - a(3)*b(2);
 c(2) = a(3)*b(1) - a(1)*b(3);
 c(3) = a(1)*b(2) - a(2)*b(1);
 return
end subroutine
```